

## BIROn - Birkbeck Institutional Research Online

Pearce, R. K. and Sánchez de la Muela, A. and Moorkamp, M. and Hammond, James O.S. and Mitchell, T. M. and Cembrano, J. and Araya Vargas, J. and Meredith, P. G. and Iturrieta, P. and Pérez Estay, N. and Marshall, N. R. and Smith, J. and Yañez, G. and Griffith, W. Ashley and MarquardtRomán, C. and StantonYonge, A. and Núñez, R. (2020) Reactivation of fault systems by compartmentalized hydrothermal fluids in the Southern Andes revealed by magnetotelluric and seismic data. *Tectonics* 39 (12), e2019TC005997. ISSN 0278-7407.

Downloaded from: <https://eprints.bbk.ac.uk/id/eprint/41528/>

*Usage Guidelines:*

Please refer to usage guidelines at <https://eprints.bbk.ac.uk/policies.html>  
contact [lib-eprints@bbk.ac.uk](mailto:lib-eprints@bbk.ac.uk).

or alternatively

1    Reactivation of fault systems by compartmentalized hydrothermal  
2    fluids in the Southern Andes revealed by magnetotelluric and seismic  
3    data

4

5    R. K. Pearce <sup>1</sup>, A. Sánchez de la Muela <sup>2,1</sup>, M. Moorkamp <sup>3</sup>, J. O. S., Hammond <sup>2</sup>, T. M. Mitchell <sup>1</sup>, J.  
6    Cembrano <sup>4</sup>, J. Araya Vargas <sup>4,5</sup>, P. G., Meredith <sup>1</sup>, P. Iturrieta <sup>6</sup>, N. Pérez Estay <sup>5</sup>, N. R. Marshall <sup>7</sup>, J.  
7    Smith <sup>8</sup>, G., Yañez <sup>4</sup>, W. Ashley Griffith <sup>9</sup>, C. Marquardt-Román <sup>4</sup>, A. Stanton-Yonge <sup>1,4</sup>, R. Núñez <sup>4</sup>

8

9    <sup>1</sup> Earth Science, University College London, London, United Kingdom

10    <sup>2</sup> Department of Earth and Planetary Sciences, Birkbeck, University of London, London, United  
11    Kingdom

12    <sup>3</sup> Department of Earth and Environmental Sciences, Ludwig Maximilians University of Munich,  
13    Munich, Germany

14    <sup>4</sup> Dept. Ingeniería Estructural y Geotécnica, Pontificia Universidad Católica de Chile, Santiago, Chile

15    <sup>5</sup> Centro de Excelencia en Geotermia de los Andes (CEGA), Universidad de Chile, Santiago, Chile

16    <sup>6</sup> Helmholtz Centre Potsdam, GFZ German Research Centre for Geosciences, Potsdam, Germany

17    <sup>7</sup> Department of Earth Sciences, University of Oxford, Oxford, United Kingdom

18    <sup>8</sup> Division of Geological and Planetary Sciences, California Institute of Technology

19    <sup>9</sup> School of Earth Sciences, Ohio State University, Columbus, OH, USA

20

21    **Key Points:**

22

23        • In the Andean volcanic arc, margin-parallel and blind oblique fault systems control volcanic,  
24        hydrothermal and ore-porphyry processes

25

26        • Subsurface conductivity structure and seismicity show a WNW-trending active fault in the  
27        Andean Southern Volcanic Zone

28

29        • Results show magmatic/hydrothermal fluids are compartmentalised by local faults, and  
30        elevated fluid pressures promote fault reactivation

31

32

33    Corresponding author: R. K. Pearce, [r.pearce.11@ucl.ac.uk](mailto:r.pearce.11@ucl.ac.uk)

## 34 Abstract

35

36 In active volcanic arcs such as the Andean volcanic mountain belt, magmatically-sourced  
37 fluids are channelled through the brittle crust by faults and fracture networks. In the Andes,  
38 volcanoes, geothermal springs and major mineral deposits have a spatial and genetic  
39 relationship with NNE-trending, margin-parallel faults and margin-oblique, NW-trending  
40 Andean Transverse Faults (ATF). The Tinguiririca and Planchón-Peteroa volcanoes in the  
41 Andean Southern Volcanic Zone (SVZ) demonstrate this relationship, as their spatially  
42 associated thermal springs show strike alignment to the NNE-oriented El Fierro Thrust Fault  
43 System. We constrain the fault system architecture and its interaction with volcanically  
44 sourced hydrothermal fluids using a combined magnetotelluric (MT) and seismic survey that  
45 was deployed for 20 months. High conductivity zones are located along the axis of the active  
46 volcanic chain, delineating fluids and/or melt. A distinct WNW-trending cluster of seismicity  
47 correlates with resistivity contrasts, considered to be a reactivated ATF. Seismicity occurs  
48 below 4 km, suggesting activity is limited to basement rocks, and the cessation of seismicity  
49 at 9 km delineates the local brittle-ductile transition. As seismicity is not seen west of the El  
50 Fierro fault, we hypothesize that this structure plays a key role in compartmentalizing  
51 magmatically-derived hydrothermal fluids to the east, where the fault zone acts as a barrier  
52 to cross-fault fluid migration and channels fault-parallel fluid flow to the surface from depth.  
53 Increases in fluid pressure above hydrostatic may facilitate reactivation. This site-specific case  
54 study provides the first three-dimensional seismic and magnetotelluric observations of the  
55 mechanics behind the reactivation of an ATF.

56

57

## 58 1 Introduction

59

60 The ascent of magmatically sourced fluids through the brittle crust is facilitated by inherited planes of  
61 weakness, such as lithospheric scale fault systems (Cembrano and Lara, 2009; Nakamura, 1977; Shaw,  
62 1980). Within these fault systems, highly permeable networks of inter-connected fault damage zones  
63 act as fluid conduits (Faulkner et al., 2010). Conversely, variations in pressure, temperature and  
64 composition of fluids in the fracture network can lead to fracture sealing and cementation, as mineral

65 precipitation during fluid transport decreases the permeability of the fault core (e.g. Cox, 2005;  
66 Micklethwaite et al., 2010). This causes the maximum flow direction to orient parallel to the fault  
67 plane (Caine et al., 1996; Faulkner et al., 2010). Simultaneously, the migration and accumulation of  
68 fluids within these fault systems play a key role in the nucleation of earthquakes, as increased pore  
69 fluid pressures reduce the effective normal stress projected on a fault plane, consequently increasing  
70 its probability of failure (Cox, 2010, 2016; Roquer et al., 2017; Sibson, 1985). These interdependent  
71 processes result in episodic and anisotropic migration of fluids within fault zones, along with the  
72 heterogeneous distribution of hydro-mechanical properties therein (Cox, 2010; Rowland and Sibson,  
73 2004; Sibson, 1996, 2004).

74

75 In an active volcanic arc, this complex interaction between hydrothermal fluids and structural systems  
76 can significantly influence tectono-magmatic processes, such as the distribution of volcanoes  
77 (Cembrano and Lara, 2009; Nakamura, 1977; Sielfeld et al., 2017; Tibaldi, 2005), the emplacement of  
78 ore deposits and plutons (Hedenquist and Lowenstern, 1994; Piquer et al., 2016), the localized  
79 structural and geochemical development of geothermal springs and fumaroles (Sanchez et al., 2013;  
80 Sibson, 1996; Tardani et al., 2016; Veloso et al., 2019) and the location, magnitude, frequency and  
81 timing of crustal seismicity (Cox, 2016). Geophysical studies can image these active structural and  
82 hydromagmatic systems in order to map their architecture as a function of depth. In particular,  
83 magnetotelluric (MT) surveys map electrical conductivity domains that are commonly related to the  
84 presence or absence of fluids with different degrees of salinity or partial melt at a crustal scale  
85 (Pommier, 2014; Simpson and Bahr, 2005). When combined with local seismic hypocenter locations,  
86 the spatial coherency of anomalous conductors and seismogenic features can reveal interacting  
87 hydrothermal fluids and seismically active fault systems in a volcanic regime (e.g. Becken and Ritter,  
88 2012; Bertrand et al., 2012; Wannamaker et al., 2009).

89

90 The overall aim of this study is to image and constrain the architecture of a major fault system within  
91 a volcanic arc using a combined magnetotelluric (MT) and seismicity survey. This site-specific case  
92 study will be used to analyse the relationship between actively deforming faults, and their role in  
93 fluid transport and storage throughout the upper crust. This objective was achieved by conducting  
94 spatially and temporally-overlapping MT and seismic surveys in a field study area within the Andean  
95 Southern Volcanic Zone (SVZ), that encompasses the Tinguiririca and Planchón-Peteroa Volcanic  
96 complexes (70.4 – 70.9°W and 34.65 – 35.2°S). In this region, significant evidence of interdependent  
97 tectonic-hydrothermal processes has been reported. A prominent geothermal reservoir found at the  
98 western flank of the Tinguiririca volcanic complex has been considered for geothermal energy

99 exploitation (Aravena et al., 2016; Benavente et al., 2016; Clavero et al., 2011; Pritchard et al., 2013).  
100 The Planchón-Peteroa volcanic complex (PPVC), which has been episodically on yellow alert due to  
101 degassing and ash expulsion events since 2011 (Aguilera et al., 2016; GVP, 2020), demonstrates a NNE-  
102 strike alignment of eruptive vents and proximal geothermal springs along the major El Fierro Fault  
103 System (EFFS) that outcrops within the field area (Giambiagi et al., 2019; Mescua et al., 2013; Pavez  
104 et al., 2016; Piquer et al., 2019). The region of the SVZ is of particular interest due to the presence of  
105 both convergent margin-parallel fold-thrust belt systems such as the EFFS, and margin-oblique WNW  
106 and ENE trending features, referred to as Andean Transverse Faults (ATF) (Cembrano and Lara, 2009;  
107 Katz, 1971). Although significant geological and geochemical evidence indicates that these margin-  
108 oblique structures exert control on volcanism (Cembrano and Lara, 2009; Lara et al., 2004; Piquer et  
109 al., 2019; Sielfeld et al., 2017), hydrothermal system dynamics (Lara et al., 2004; Sanchez-Alfaro et al.,  
110 2015) and ore-porphyry deposition (Chernicoff et al., 2002; Sillitoe, 1997), the subsurface interaction  
111 of these processes are poorly understood.

112

## 113 2 Margin parallel and oblique fault systems in the Southern Andes

114

115 The Andes comprise of a volcanically active mountain belt along the western margin of South America  
116 between latitudes 18-46°S, which have formed from the roughly eastward convergence and  
117 subduction of the oceanic Nazca Plate beneath the South American Plate since the Jurassic (ca 180  
118 Ma) (Charrier et al., 2007; Mpodozis and Cornejo, 2012; Pardo et al., 2009; Ramos, 2010). Since the  
119 Miocene (<20 Ma), orogenic uplift was coupled with intense volcanism and the formation of an  
120 eastward migrating volcanic arc. The relative plate convergence velocity of 6.6cm/year has had a trend  
121 of N78°E since the Holocene (<12Ma) (Angermann et al., 1999). The Andean western margin is  
122 characterized by: (a) over 200 Pleistocene-Holocene stratovolcanoes throughout its volcanic arc (60  
123 of which have been active during the Holocene) (Stern, 2007), (b) mega-thrust earthquakes that reach  
124 magnitudes >Mw 8, such as the Mw 9.5 Valdivia and Mw 8.8 Maule earthquakes in 1960 and 2010,  
125 respectively (Bonali et al., 2013), (c) giant Cu-Au-Ag porphyry ore deposits (Chernicoff et al., 2002;  
126 Sillitoe, 1997), and (d) up to 16,000 MWe of potential high enthalpy geothermal resources (Aravena  
127 et al., 2016; Sanchez-Alfaro et al., 2015). Figure 1 shows the major NNE trending margin-parallel  
128 volcanic arc, and the distribution of ore deposits, geothermal springs and oblique lineaments along  
129 the Southern Andes. Throughout this region, volcanoes, geothermal springs and the locations of major  
130 mineral deposits are spatially coherent with the first-order NNE oriented structural systems in the  
131 High Andes (Ramos, 2010). An exception is the region between 28 - 33°S referred to as the Pampean  
132 Flat Slab Segment, where shallow subduction angles prevented the formation of a mantle wedge,

133 resulting in a break in the volcanic arc (Mpodozis et al., 1989). The porphyry-copper provinces are  
134 younger in age towards the south; the metallogenic belts in the north, including the Chuquicamata  
135 and Escondida mines, formed during the late-Eocene – early-Oligocene (38 – 35 Ma) (Richards et al.,  
136 2001), whereas the southernmost mapped mine, El Teniente, is from an ore province that formed  
137 during late-Miocene – early-Pliocene (10 – 4 Ma) (Piquer et al., 2015).

138

139 Second order NW-trending transverse structural domains that cross-cut the volcanic arc have been  
140 observed throughout the Andes, and are considered to be pre-Andean, inherited basement faults  
141 (e.g. Katz, 1971; Lara et al., 2006; Melnick and Echtler, 2006; Piquer et al., 2017; Yáñez et al., 1998).  
142 These seismically active Andean Transverse Faults (ATF) (Aron et al., 2015; Sielfeld et al., 2019;  
143 Stanton-Yonge et al., 2016) accommodate part of the deformation arising from oblique convergence  
144 (Perez-Flores et al., 2016; Stanton-Yonge et al., 2016), are spatially and genetically associated with  
145 massive to medium scale ore deposits (e.g. Chernicoff et al., 2002; Mpodozis and Cornejo, 2012;  
146 Piquer et al., 2015) and are believed to control the seismic segmentation of the plate interface  
147 (Melnick et al., 2009).

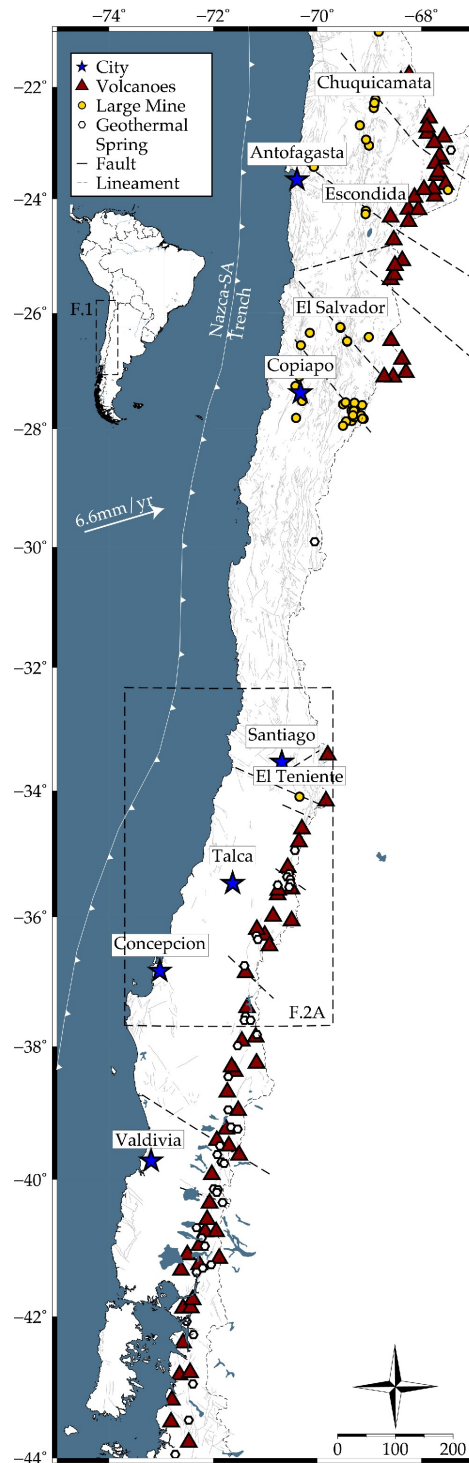
148

149 Within the arc domain, ATF are considered to influence magmatic processes, as volcanic and intrusive  
150 body emplacement show alignment with the strike of ATF domains (Acocella et al., 2011; Cembrano  
151 and Lara, 2009; Viramonte et al., 1984). These ATF are enigmatic due to their WNW orientation with  
152 respect to the current plate convergence vector, which promotes a bulk transpressive stress regime.  
153 This makes them unfavourable for dilation that facilitates magma ascent through the crust (Cembrano  
154 and Lara, 2009). However, these WNW-trending faults are nearly optimally oriented to accommodate  
155 sinistral-reverse displacement (Stanton-Yonge et al., 2016). Recent investigations have determined  
156 that these structures store over-pressurized fluids derived from deep magmatic roots, thus impacting  
157 the architecture and distribution of active volcanic and hydrothermal systems across the Andes  
158 (Sanchez et al., 2013; Sielfeld et al., 2019; Tardani et al., 2016; Veloso et al., 2019; Wrage et al., 2017).  
159 Furthermore, the interaction between NNE-trending fault systems and ATF at the SVZ controls the  
160 conditions required to develop and sustain a shallow hydrothermal system, where fluids within  
161 conduits associated with ATF are stored and over-pressurized (Perez-Flores et al., 2017; Roquer et al.,  
162 2017).

163

164 The intersection of major NNE oriented fault systems and the potentially blind, discrete WNW-  
165 trending ATF domains occur across all latitudes of the Andes, showing an along-strike spatial control  
166 of major mineral deposits (Katz, 1971; Sillitoe, 1997). Sillitoe (1997) and Piquer et al. (2019) suggested

167 that hydrothermal minerals related to porphyry copper deposits of central Chile are formed at such  
 168 intersections.



169  
 170 *Figure 1. Map of the Andean volcanic chain between latitudes 21.5° and 44°S. See legend in top left*  
 171 *corner for description of symbols. Localities of active volcanoes are sourced from the Smithsonian*  
 172 *Institute Holocene Volcanic database, geothermal areas from (2016), faults and major mines from*  
 173 *Sernageomin (2003), northern lineaments (21.5-28°S) sourced from Richards et al. (2001), southern*

174 *lineaments from Cembrano and Lara (2009), and plate vector from Angermann et al. (1999). The frame*  
175 *overlying the map between latitudes 32-38°S indicates the location of Figure 2a.*

176

177 As the surface expressions of the ATF are limited to a few scarce outcrops (Lara et al., 2004; Perez-  
178 Flores et al., 2016), they are mostly inferred from kilometre-scale topographic lineaments (Cembrano  
179 and Lara, 2009; Giambiagi et al., 2019; Moreno, 1976; Piquer et al., 2016), major magnetic anomalies  
180 (Yáñez et al., 1998) and alignment of seismicity and volcanic morphological features (Aron et al., 2015;  
181 Lara et al., 2004; Sielfeld et al., 2017).

182

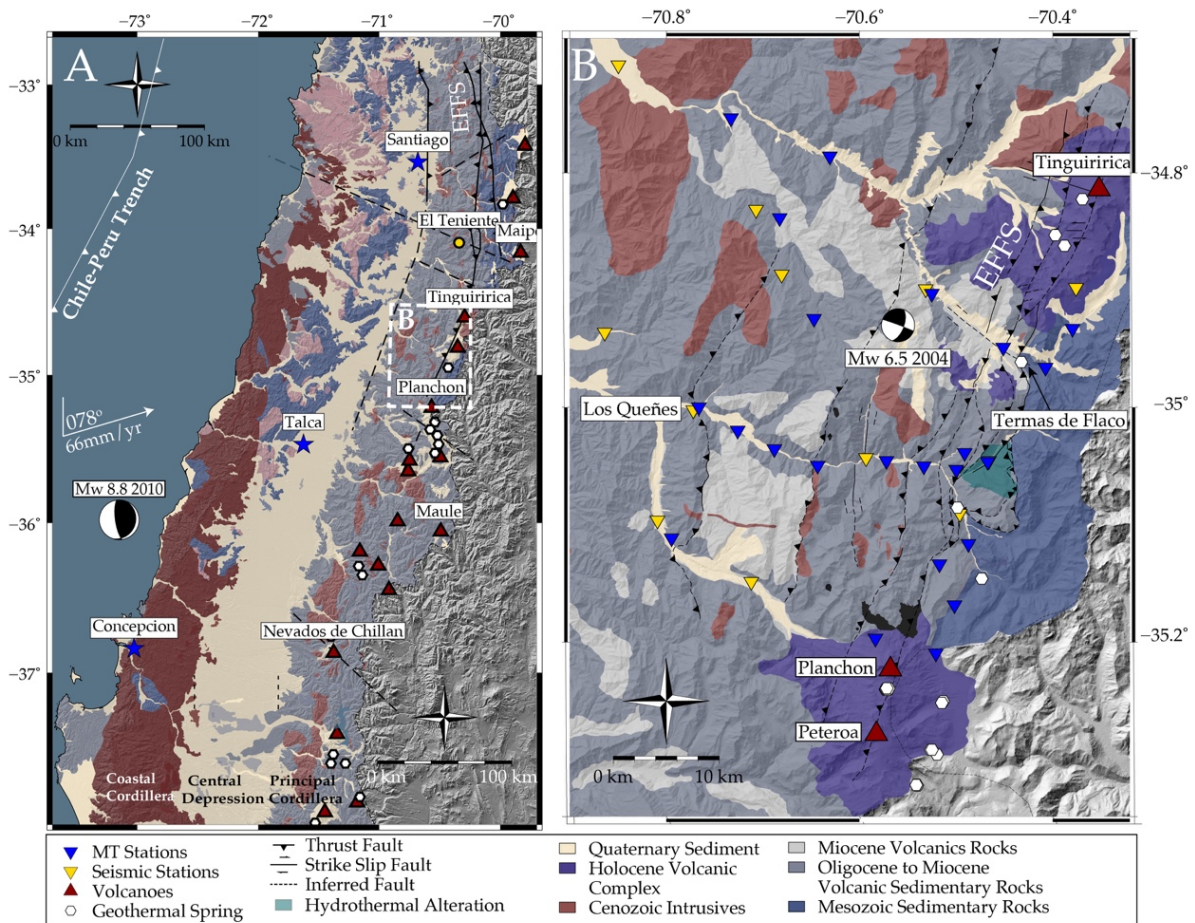
183 The setting of this study is the Andean SVZ, which features margin parallel fault systems, margin-  
184 oblique ATF system, and fault-strike aligned volcanic complexes. The geological, geophysical and  
185 geochemical signatures of these domains indicate that these faults and volcanic systems have  
186 interdependently evolved during the orogenesis of the Andes, however their interaction at depth  
187 remains unresolved. This study provides a high-resolution 3D model of an area characterized by these  
188 structural and volcanic systems, with the aim to improve our understanding of their nature within  
189 upper crustal depths.

### 190 3 Regional context and geology

191

192 The Andes are segmented from north to south into Northern, Central, Southern and Austral Volcanic  
193 Zones, due to the latitudinal variation of altitude, crustal thickness, convergence rate, plate coupling,  
194 volcanism and climate (Ramos, 2010). The selected field area for this study is in the Southern Volcanic  
195 Zone (SVZ) in the Principal Cordillera (Figure 2A). In this region, the main morpho-tectonic features of  
196 the Chilean Andes are the western Coastal and eastern Principal Cordillera, which are divided by the  
197 Central Depression (Figure 2A) (Charrier et al., 2015; Ramos et al., 2014). The EFS is the major  
198 structural feature in the region, which thrusts the Miocene volcanic sequences eastward over an  
199 exposed sequence of Mesozoic sedimentary units (Farias et al., 2010). The surveyed study area is  
200 located at the western limit of the Chilean Principal Cordillera at this Meso-Cenozoic boundary (Figure  
201 2B). This boundary is characterized by a heat flow regime of 200mW/m<sup>2</sup>, which is anomalously high  
202 compared to the heat flow regime of 60mW/m<sup>2</sup> in the surrounding western and north-western Andes  
203 (Benavente et al., 2016). This high heat flow gradient occurs as the eastward migrating volcanic arc is  
204 partially situated beneath the Principal Cordillera. Thus, volcano-magmatic processes, such as the  
205 development of major stratovolcanoes and geothermal fluid outflow springs, are concentrated in the

206 High Andes (Figure 1) (Benavente et al., 2016). The Tinguiririca geothermal outflow spring, as well as  
 207 the Planchón-Peteroa volcanic complex are within the limits of the geophysical survey grid (Figure 2B).  
 208



209  
 210 *Figure 2. A) Regional scale geology of the Andes of central-southern Chile and of the Southern Volcanic*  
 211 *Zone. See legend for a description of all symbols. The geological units and the El Teniente mine location*  
 212 *are from Sernageomin (2003), and focal mechanisms of the Maule and Teno earthquakes are after*  
 213 *Ekstrom et al. (2012). Frame labelled B in A indicates the location of Figure 2B. B) Local geological map*  
 214 *of the field study area from Núñez Tapia (2018) and distribution of magnetotelluric and seismic*  
 215 *stations within the geophysical survey grid. Digital Elevation Model (DEM) from PALSAR (2011).*  
 216

### 217 3.1 Hydrothermal & magmatic systems of the Tinguiririca & Planchón-Peteroa 218 Stratovolcanic Complexes 219

220 The Tinguiririca volcanic complex (Figure 2B) is a Holocene cluster of 10 scoria cones that overlay a  
 221 lower to middle Pleistocene plateau of andesitic lavas, directly above the NNE-trending EFFS (Stern,  
 222 2007). Tinguiririca's potential for geothermal exploitation has been evaluated with magnetotelluric  
 223 (Lira Martínez, 2011), seismic (Clavero et al., 2011), geochemical (Benavente et al., 2016) and borehole

224 methods (Droguett et al., 2012), revealing a deep geothermal reservoir with a volume of 5 - 25 km<sup>3</sup>  
225 contained by a low-resistivity hydrothermally-altered argillic clay cap at 3-6 km depth (Aravena et al.,  
226 2016; Lira Martínez, 2011). Current thermal activity in proximity of Tinguiririca include high elevation  
227 fumaroles and lowland chloric springs, such as the major outflow spring Termas de Flaco, a sulfur-rich  
228 mud pool that is commercially exploited (Figure 2B) (Benavente et al., 2016; Pavez et al., 2016). The  
229 geochemical signatures of these springs and high altitude fumaroles indicate that the reservoir's  
230 temperatures range from 230 – 250°C, bearing trace elements of shallow meteoric aquifers and deep  
231 source magmatic gasses (Aravena et al., 2016; Benavente et al., 2016; Pavez et al., 2016). Fumarolic  
232 discharge also shows typical signatures of a hydrothermal system, including water vapour,  
233 concentrations of CH<sub>4</sub>, H<sub>2</sub> and H<sub>2</sub>S and magmatic arc type gases (Benavente et al., 2016). Based on  
234 these observations it is interpreted that a 2-6 km deep reservoir related to the Tinguiririca volcano is  
235 recharged by the circulation of shallow meteoric and deep magmatic fluids (Benavente et al., 2016;  
236 Giambiagi et al., 2019; Pavez et al., 2016).

237

238 The Planchón-Peteroa volcanic complex (PPVC) (Figure 2B) consists of a series of Pleistocene -  
239 Holocene stratovolcanoes with two main volcanic centres: Planchón (14 ka) and Peteroa (<7 ka) (Tassi  
240 et al., 2016). Like the Tinguiririca volcano, these volcanic edifices are emplaced along the trace of the  
241 EFFF. The composition of the PPVC progresses from earliest stage basaltic lavas to bimodal basaltic-  
242 andesitic and dacitic magmas extruded as subplinian explosions (Stern, 2007). Fumarolic discharge  
243 and acid crater lakes are proximal to the edifice, with chemical signatures of a hydrothermal system  
244 recharged by meteoric waters, that also bear He signatures indicative of deeper magma-derived fluid  
245 sources (Benavente et al., 2016). A phreatic eruption accompanied by ash discharge occurred from  
246 August, 2010 - June 2011, placing Planchón-Peteroa on yellow alert eruption warning that is still in  
247 place. Subsequent tephra fall contained altered Fe-oxides and Cu-minerals but no juvenile magmatic  
248 constituents, indicating that hydrothermal fluid migration drove the phreatic eruption and tephra  
249 production. This eruption stage was followed by sporadic ash and vapour emission, which were  
250 hydrothermally sourced, and bore traces of deep oxidized magmatic fluids. These magmatic traces,  
251 including SO<sub>2</sub>, HCl and HF, contained signatures of a highly degassed (old) magmatic body (Tassi et al.,  
252 2016). It has since experienced sporadic events of degassing, water-vapor expulsion and shallow  
253 seismic tremors, the most notable of which are a Mw 4 earthquake that occurred 4-7 km beneath the  
254 summit on July 8th, 2017, and an explosive ash emission in September 2018 (GVP, 2020).

255

### 256 3.2 Faulting, kinematics and hydrothermal alteration

257

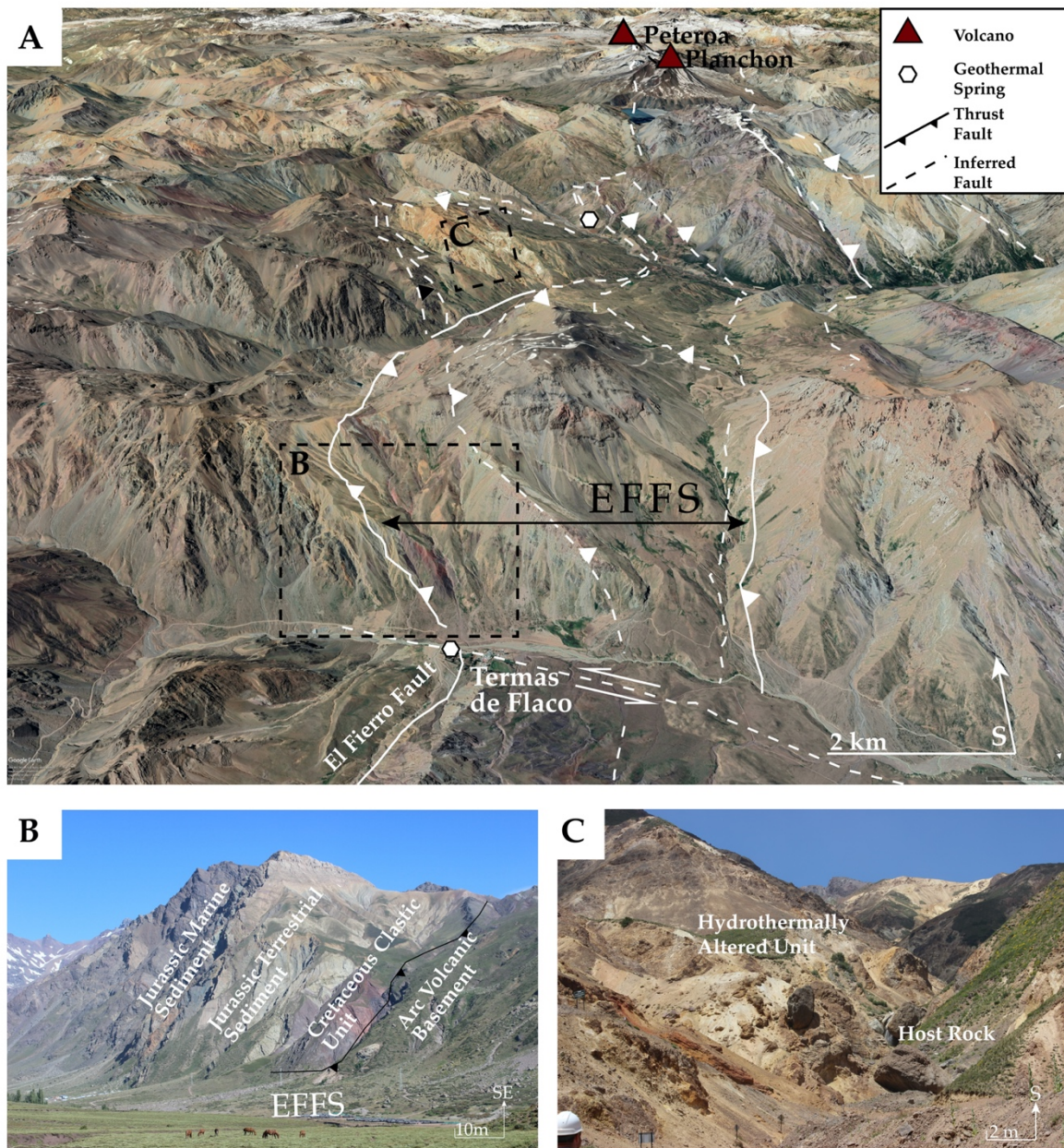
258 The largest structural feature in the study area is a segment of the NNE-trending, 200km long El Fierro  
259 Fault System (EFFS), a steeply-dipping, reverse fault that formed during the late-Eocene to Oligocene.  
260 Reverse faulting deformation initiated when thickening of the lower crust was assisted by magmatic  
261 softening, and arc rocks were subsequently displaced eastward and uplifted along this fault (Charrier  
262 et al., 2002; Godoy and Lara, 1994; Gow and Walshe, 2005). Structural analysis of this fault system  
263 suggests that, while the dominant structure formed from reverse faulting, its current kinematics is  
264 dextral strike slip under regional transpression (Giambiagi et al., 2019). Outcropping fault strands of  
265 the EFFS show distinct alignment with volcanic and geothermic features in the area (Figure 3A).  
266 Additionally, significant hydrothermal alteration is seen in the Oligocene to Miocene volcanic and  
267 sedimentary rocks, spatially related to the hanging wall of the EFFS (Figure 3C). The alteration in this  
268 zone is of phillite-argillic type, with pervasive pyrite veinlets. The alteration appears to be strongly  
269 controlled by lithology, where the more fractured and permeable units exhibit stronger alteration.  
270 Additionally, it shows evidence of a supergene alteration, which produces oxidation and leaching of  
271 sulphides (i.e. pyrite), forming limonites (Jarosite > Goethite > Hematite). This alteration is restricted  
272 to within the strands of the El Fierro fault, and the foot wall (Figure 3A & C).

273

274 Previous seismic tomography studies south of Tinguiririca volcano have inferred that the permeable  
275 damage zones of the EFFS act as channels for meteoric and magmatic derived fluids into the  
276 geothermal fields and outflow springs (Pavez et al., 2016). The presence of fluids in a porous and  
277 fractured media in the EFFS was inferred due to the presence of high  $V_p/V_s$  ratios. When combined  
278 with geochemical analyses of fumarolic discharges (Benavente et al., 2016), these results suggest that  
279 an active deep andesitic magmatic system underlies an upper hydrothermal zone located at 2 – 3 km  
280 depth. These studies conclude that a magmatic reservoir is emplaced between 6 - 9 km depths (3 – 6  
281 km below sea level in the research article), and that the EFFS is a conduit for fluid mobility. This  
282 interpretation has recently been debated by Giambiagi et al. (2019), who combined paleostress  
283 analysis, structural mapping and boundary element modelling methods to characterize the Tinguiririca  
284 geothermal fields, specifically the mechanisms that control fluid migration in this hydromagmatic  
285 system. They state that a blind NNE oriented strike-slip fault at 2.5 km depth within the EFFS volume  
286 controls the migration of fluids, due to strong directional permeability that occurs at the fault  
287 intersection with surrounding strands of the EFFS. This blind fault acts to localize hydrothermal fluid  
288 circulation, which in turn increases the fault's probability of failure due to increased pore fluid  
289 pressures along the fault plane. This became apparent when a seismic swarm in 2010 highlighted the  
290 geometry of this blind fault plane (Lira Martínez, 2011). The 2010 seismic swarm is considered to be  
291 related to local stress redistribution from the 2004 6.5 Mw earthquake (Figure 2B). From this event,

292 along with local paleostress analysis in the Tinguiririca valley, an ESE oriented sinistral strike slip  
 293 regime is assumed to dominate this region (Giambiagi et al., 2019).

294



295

296

297 *Figure 3. A) Satellite image of the field area looking SSE, displaying the primary features of interest;*  
 298 *the trace of El Fierro thrust fault system is taken from Pavez et al. (2016), and inferred sinistral strike-*  
 299 *slip faults (potential ATF) from Giambiagi et al. (2019). The larger and smaller black frames in A*  
 300 *indicate the locations of B and C respectively. B) Photo showing the high angled El Fierro fault plane*  
 301 *creating the unconformity between the Jurassic sediments and Quaternary volcanoclastics. C) Photo*  
 302 *showing hydrothermally altered, Oligocene-Miocene volcanic host rock at the EFFS fault zone.*

303

## 304 4 Geophysical Data Acquisition and Processing

305

306 Magnetotellurics (MT) is a geophysical method that uses naturally occurring electromagnetic fields to  
307 estimate the electrical conductivity structure of the subsurface (Simpson & Bahr, 2005; Chave & Jones,  
308 2012). Coupled with MT, precise hypocentre locations in seismically-active areas can be used to infer  
309 the location, geometry and distribution of active faults that may interact with crustal fluids (Held et  
310 al., 2016; Ingham et al., 2009; Legrand et al., 2011; Wannamaker et al., 2009). For these reasons, this  
311 study combines seismic hypocenters with a 3D of conductivity structure.

312

### 313 4.1 Magnetotelluric Survey, Data Processing and Inversion

314

315 In magnetotellurics, naturally occurring electromagnetic fields incident on the Earth's surface are  
316 passively and independently measured as a continuous time series of two horizontal electric  
317 components,  $E_x$ ,  $E_y$ , and two horizontal magnetic components,  $H_x$  and  $H_y$ . When converted into the  
318 frequency domain, the response of the electric current to a varying magnetic field is quantified as the  
319 complex impedance tensor as a function of frequency,  $Z_w$ . The impedance responses are then used  
320 to model conductivity variations of the Earth's subsurface through the relation  $E = ZH$  (Simpson and  
321 Bahr, 2005).

322

323 The field campaign involved the collection of 26 broadband induction coil MT sites with approximately  
324 5 km spacing in a 40 km<sup>2</sup> field area (Figure 2B). At all MT stations, the North-South ( $x$ ) and East-West  
325 components ( $y$ ) of the electric and magnetic fields were independently measured, as well as a vertical  
326 component of the magnetic field. MT data were collected using Metronix ADU-07e systems equipped  
327 with MFS-06e or MFS-07e coils. The experiment sampled at 1024 Hz for an initial 30 minutes, after  
328 which data was collected at a 128 Hz sampling rate for 48 hours. As the features of interest in this  
329 study are concentrated in the eastern limits of the surveyed area, namely the EFFE and the along-  
330 strike Tinguiririca and Planchón-Peteroa volcanic complexes, the MT grid has a dense NS oriented  
331 transect in this sector, while three EW oriented transects were deployed to act as regional controls.  
332 The data processing method used was the Bounded Influence Remote Referencing (BIRRP) program  
333 (Chave, 1989; Chave and Thomson, 2003). This well-established MT data processing algorithm uses  
334 statistically robust techniques and remote referencing to yield the impedance responses at selected  
335 frequencies. Of the completed 26 sites, data from 3 stations have been discarded due to irreparably  
336 poor data quality attributed to cultural and natural noise contamination, such as electric dipole  
337 interference or current channelling respectively. Some datasets also feature Galvanic Distortion,

338 which is caused by near-surface conductivity heterogeneities at the measurement site (Bibby et al.,  
339 2005). The period bands affected by high levels of artificial noise were masked by assigning high error  
340 values to the data points in order to reduce the impact of noisy data on the inversion results. An  
341 example of this effect is observed in the YX component of the 3 – 20 s period band of station 2 in  
342 Figure 4. The 3D inversion of the 23 station MT grid was performed with a quasi-Newton optimization  
343 method that minimizes the data misfit and Tikhonov-type regularization parameter (Avdeev and  
344 Avdeeva, 2009; Avdeev, 2005). The algorithm uses joint inversion methods to correct for galvanic  
345 distortion inherent in the data. The distortion correction multiplies the frequency-independent, real  
346 valued distortion matrix,  $C$ , to the complex, frequency-dependent impedance tensor in the form  
347  $Z_{obs}=CZ$  (Avdeev, 2005).

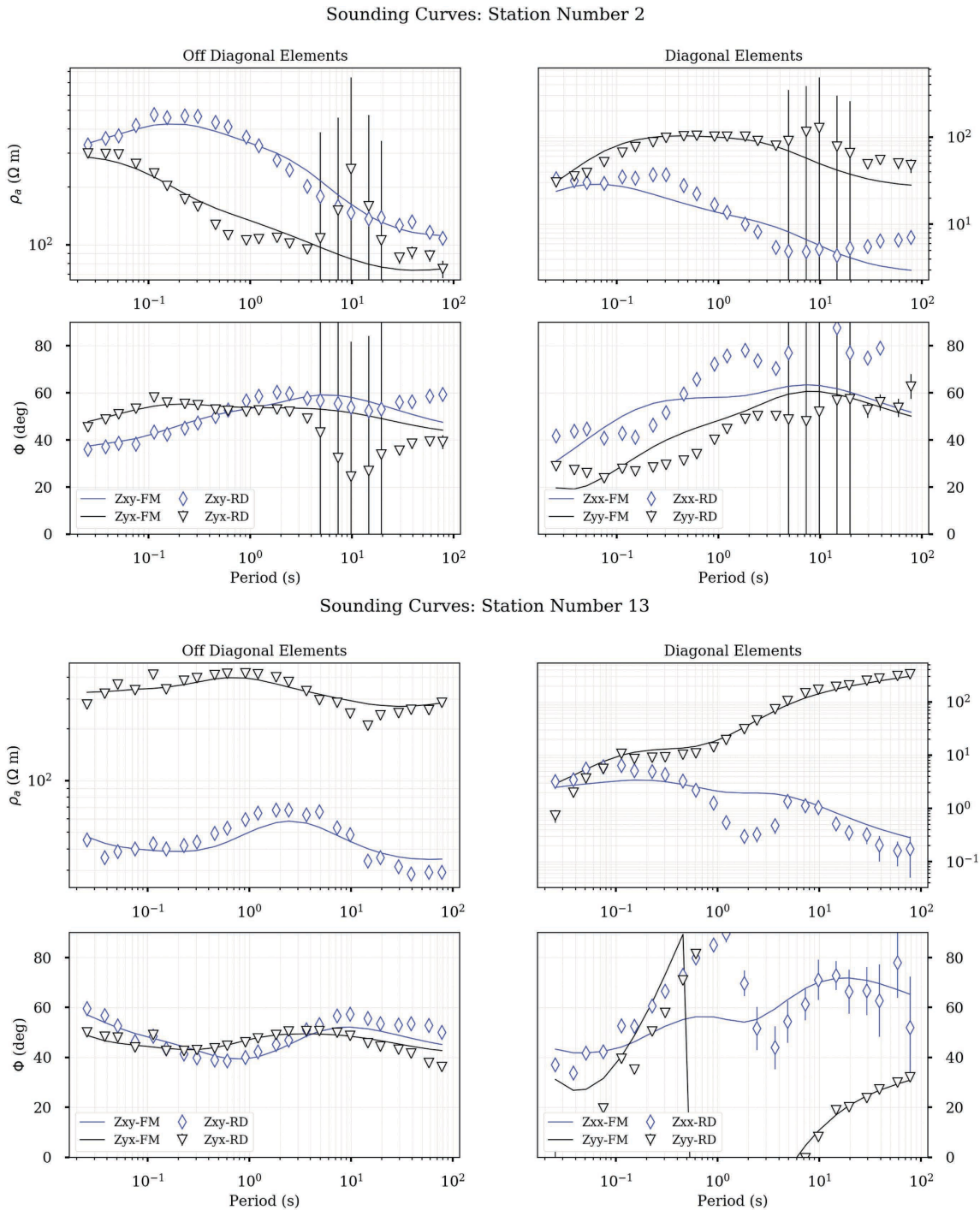
348

349 The initial model mesh comprised 80x80x30 cells, with cell dimensions of 1000 m x 1000 m x 100 m  
350 that was increased by a factor 1.1 times the vertical cell length per layer. The inversion was conducted  
351 with an error floor of 5% for the impedance datasets, and a large regularization parameter that was  
352 reduced by one order of magnitude per inversion run. Homogeneous meshes with initial  
353 conductivities 100, 500 and 1000  $\Omega\text{m}$  were used as starting models to conduct full inversions, and to  
354 produce layered models based on the 1D inversion of the average of the dataset. The layered models  
355 all resulted in a mesh of an overall 500  $\Omega\text{m}$  resistivity with a 50 – 100  $\Omega\text{m}$  layer between 8 - 14km. This  
356 layered model was the starting mesh for the final model that was selected for further analysis. The  
357 final preferred model, which was obtained after 800 iterations, reduced the RMS from a value of 9 to  
358 1.55. The conductivity structure that emerged in this model was also observed in models with other  
359 initial conductivities, which supports the robustness of the result. While the RMS is a good overall  
360 measure of the fit between the inversion model and the real data, we also examine the closeness  
361 between the sounding curves of both datasets for individual stations (Miensopust et al., 2013).

362

363 An example of the real data and model fit for stations 2 and 13 is provided in Figure 4, which show the  
364 apparent resistivities and phases for all impedance components ( $Z_{xx}$ ,  $Z_{xy}$ ,  $Z_{yx}$  and  $Z_{yy}$ ) across 0.01 – 100  
365 s period bands. The results for station 2 show that the model and real datasets fit well, apparent as  
366 the inversion model data and real data (labelled FM and RD on Figure 4 respectively) closely match  
367 across all period bands. The  $Z_{yx}$  component Station 2 (Figure 4A) shows some scatter around the 3 –  
368 12 s period band, but this does not affect the inversion model due to the high errors assigned to these  
369 data points. The off-diagonal components of station 13 exhibit some Galvanic Distortion, apparent as  
370  $Z_{yx}$  is shifted to an apparent resistivity above  $Z_{xy}$  by approximately one magnitude across all period  
371 bands. As discussed, this type of Galvanic distortion is accounted for in the joint inversion by the

372 distortion tensor, and the inversion model data (FM, Figure 4B) and real data (RD, Figure 4B) fit well  
 373 despite the distortion, as was the case for all Galvanically distorted datasets (see Supplementary  
 374 Material for the real and model data fits for each station). Furthermore, sensitivity tests were carried  
 375 out to verify the robustness of each conductive structure within the model (see Supplementary  
 376 Information on these techniques).  
 377



378  
 379 *Figure 4. Magnetotelluric apparent resistivity and phase results for all impedance tensor components*  
 380 *( $Z_{xx}$ ,  $Z_{xy}$ ,  $Z_{yx}$  and  $Z_{yy}$ ) as a function of Period (s) for stations 2 and 13. Within each graph, black inverted*

381 *triangles and blue diamonds show the data and black and blue lines (FM) are the responses of our*  
382 *preferred model.*

383

#### 384 4.2 Seismic Survey and Hypocenter Location

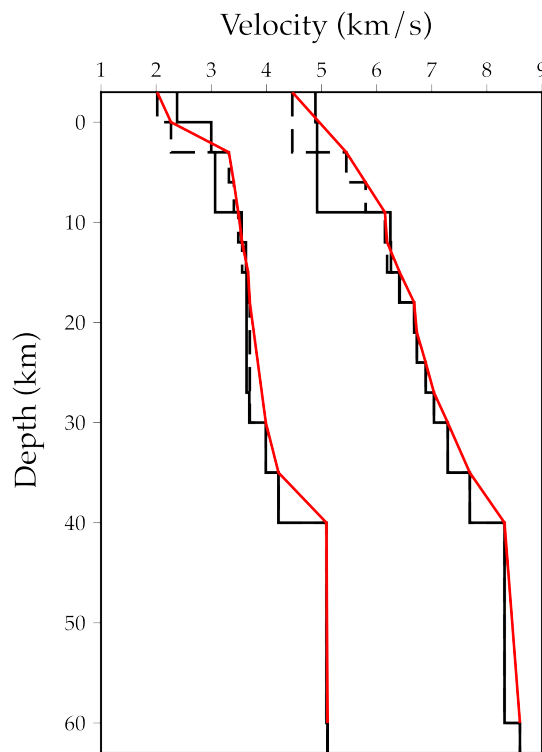
385

386 A network of 12 broadband seismometers (6 Guralp CMG-6TDs and 6 Guralp CMG- 3ESPCDs) were  
387 deployed from April 2017 until December 2018 (Hammond et al., 2017). Average inter-stations  
388 spacing was approximately 15 km, with site localities complimenting the MT stations distribution  
389 (Figure 2B). Hypocenters were automatically detected using the software package QuakeMigrate  
390 (QMigrate; <https://github.com/QuakeMigrate/QuakeMigrate>), which scans the seismic trace at each  
391 station by determining a STA/LTA onset function with high values representing phase arrivals (Drew  
392 et al., 2013; Smith et al., 2020). The onset functions are then backpropagated in a travel-time grid  
393 determining a 4D function representing the combined onsets spatially and through time. When the  
394 maximum coalescence value exceeds a user defined threshold value, an event is triggered. A marginal  
395 window, representing the expected model error, is taken about each event with the 4D coalescence  
396 stacked in the time domain to give a probability map of the earthquake location. Events are then  
397 filtered using the local- and global-gaussian error ellipses, with events with a large global-gaussian to  
398 local- gaussian ratio rejected as they represent false triggers. This procedure outputs an automated  
399 catalogue of earthquake locations, expected location uncertainties and phase arrivals. The resulting  
400 QuakeMigrate catalogue was visually inspected afterwards, to manually update P- and S-wave arrivals.  
401 These revised travel-time picks were then used to estimate hypocenters using HYPOINVERSE-2000  
402 (Klein, 2002).

403

404 Earthquake locations are sensitive to the velocity model used. We initially located a portion of our  
405 earthquakes catalogue using the velocity model calculated for the Southern Andes Volcanic Zone by  
406 Sielfeld et al. (2019). From this we obtained 205 hypocenters, with horizontal error < 2km and vertical  
407 error < 5km, azimuthal gap 87 - 336° and residuals (RMS) of 0.01 - 0.29 s. The model was then updated  
408 by iteratively inverting for the resulting locations and the initial 1-D velocity model using VELEST  
409 (Kissling et al., 1994). VELEST allowed to iteratively improve the RMS-misfit between calculated and  
410 observed travel times of each solution through updating the velocity model and relocating the  
411 earthquakes. Five different a-priori models were tested including constant velocity models and  
412 CRUST1.0. All models showed similar trends, requiring a low velocity shallow crust, but the modified  
413 1D velocity model of Sielfeld et al. (2019) proved to be the best model with the lowest RMS-misfit.

414



415

416

417 *Figure 5. P- and S-waves velocity models. The black solid lines represent the model of Sielfeld et al.*  
 418 *(2019), the black dashed lines show the velocity model updated for this study, and the red solid lines*  
 419 *represent the gradient velocity layers that reduce the sharp discontinuity that occurs at 10km depth.*

420

421 The final model used in this study is shown in Figure 5. The homogeneous velocity layers in our best  
 422 solution model were converted into gradient velocity layers, to reduce the depth-clustering effect that  
 423 sharp velocity discontinuities have on hypocentre location due to seismic rays being modelled as  
 424 refracted from discontinuities instead of realistic down-going rays with spread emergence angles  
 425 (Klein, 2002). This resulted in location of 1,369 hypocenters with a mean horizontal error of 0.92 km  
 426 and 1.68 km mean vertical error. To provide more detailed estimates of locations, the travel-time data  
 427 were reprocessed using the double-difference algorithm in HypoDD (Waldhauser and Ellsworth,  
 428 2000). This minimizes the sensitivity of source location to the velocity model and allows identification  
 429 of trends in the data with more accuracy (although with absolute location of the order of the  
 430 HYPOINVERSE-2000 results). HypoDD works on the assumption that the distance between earthquake  
 431 pairs is much less than the earthquake to station distance. With this in mind, relocation was applied  
 432 aiming to maximise the number of events located, while keeping the separation between events in a  
 433 small cluster. Each earthquake was paired with up to 30 neighbours located within 1.5 km and each  
 434 pair could have up to 24 linked arrivals. We run HypoDD in two sets of five iterations, taking initial  
 435 locations from the Hypo2000 catalogue and weighting the S phase data at 80% relative to P phases.

436 Damping was evaluated and adjusted by cluster according to the resulting condition number (CND),  
437 making sure this was between 40 and 80 and that the absolute location difference of cluster centroids  
438 was within the average errors of the Hypo2000 catalogue (Waldhauser and Ellsworth, 2000). We kept  
439 the residual threshold for the phase data (WRCT) and the maximum distance between phase pairs  
440 linked (WDCT) unconstrained for the first five iterations, letting the catalogue improve the large-scale  
441 picture freely. The next five iterations are designed to reduce outliers, by re-weighting WRCT and  
442 WDCT to 6 and 1.5 km respectively. Due to the large number of earthquakes, we computed the  
443 relocation using the conjugate gradients method, LSQR (Waldhauser and Ellsworth, 2000). In total this  
444 resulted in 1,233 linked events, with an average offset of 0.029 km; 121791 P-wave travel-time pairs  
445 and 133770 S-wave travel time pairs. The final relocated catalogue includes 951 hypocenters and is  
446 shown in Figure 6A.

447

## 448 5 Spatial distribution of resistivity anomalies and seismicity

449

450 The resolution of conductivity anomalies discussed in this section has been validated with a series of  
451 robustness tests (see supplementary material). All anomalies within the model have proved to be  
452 robust through multiple sensitivity tests, with the exception of the low-resolution region below C1  
453 (Figure 6 & 7, sensitivity tests 3 & 4).

454

455 Overall, two distinct resistivity domains can be distinguished in the study area: an eastern domain of  
456 low resistivity ( $<50 \Omega\text{m}$ , sensitivity test 16) and a western domain of high resistivity (values between  
457  $500 - 10,000 \Omega\text{m}$ , sensitivity tests 8 & 9). These two domains are best shown in cross-sections WNW-  
458 1 and WNW-2 (Figure 7), both of which are perpendicular to the general trend of the resistivity  
459 contrast and trace of the El Fierro fault system. The conductive domain is aligned in a NNE volcanic  
460 arc-parallel orientation, as has been observed in comparable MT studies in the Southern and Central  
461 Andes (e.g. Díaz et al., 2015; Held et al., 2016; Hickson et al., 2011; Kapinos et al., 2016), and the  
462 majority of seismic hypocentres are located in the eastern domain, below and to the east of the EDFS.  
463 There is a distinct lack of seismicity in the western high resistivity domain (Figures 6 & 7), and almost  
464 all of the seismicity is located in the eastern footwall of the EDFS, and below 4 km depth (figure 7,  
465 WNW-1 & WNW-2).

466

467 The eastern domain of low resistivity is segmented in the north-south orientation, populated by four  
468 distinct conductors (C1, C2, C3 and C4, sensitivity tests 1, 6, 7, 8, 12 & 13) and 2 main seismic clusters  
469 (Cls1 and Cls2) (Figure 6 & 7). The seismic cluster Cls1 is elongated in a WNW direction and within a

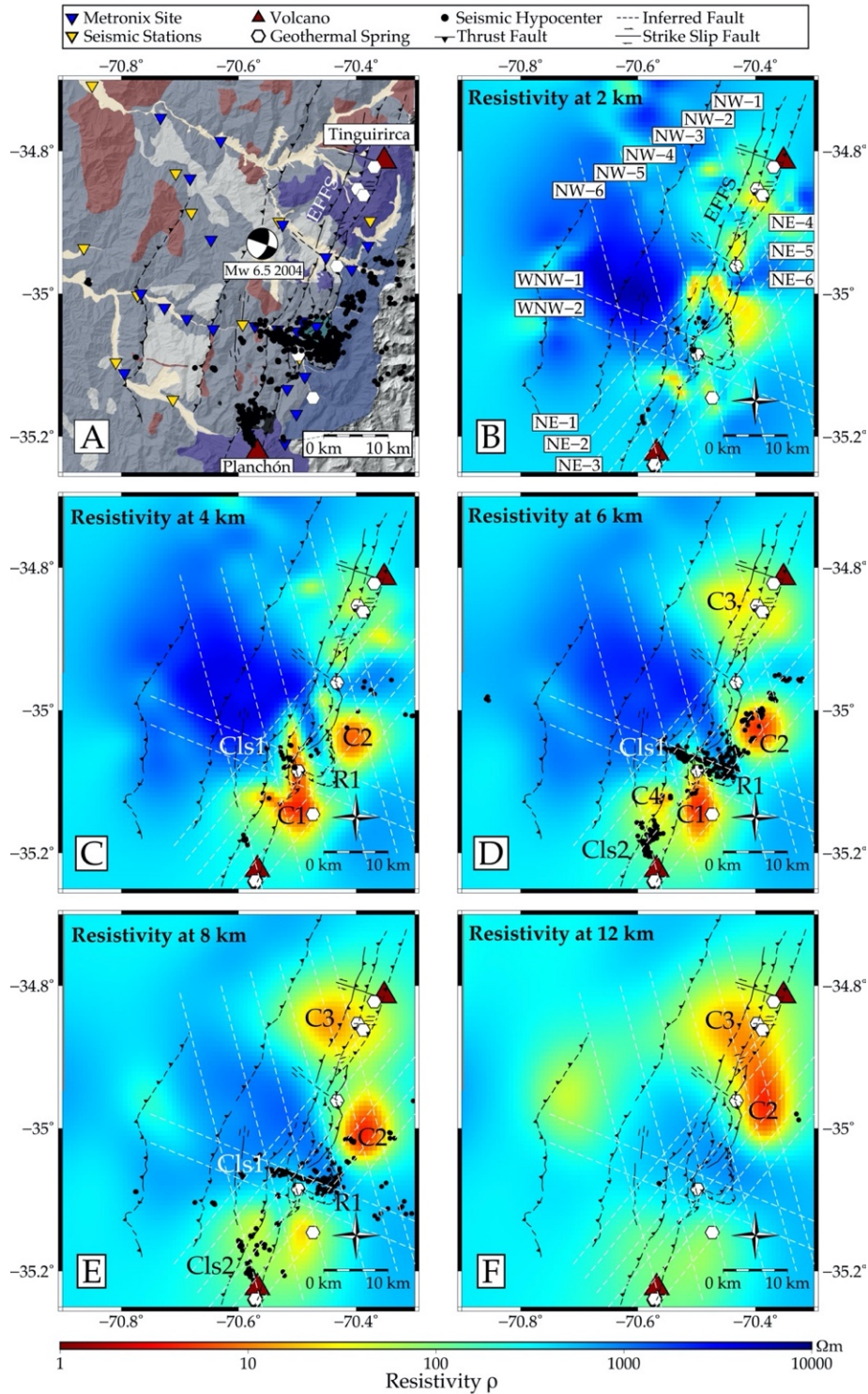
470 low conductivity (R1) region, adjacent to conductor C1 (e.g. Figure 7, cross-sections NE-1, NE-2, NE-3,  
471 NW-5, and NW-6 compared to WNW-1) that is located NE of the Planchón-Peteroa volcanoes at a  
472 depth of 4 – 8 km. At 6 km (Figure 6D), the distinct WNW alignment of seismic cluster Cls1 extends for  
473 approximately 10 km length, aligning with an abrupt boundary between C1 and a WNW oriented  
474 resistive corridor (conductivity ranges 500 - 1,000  $\Omega\text{m}$ ), R1 (sensitivity tests 10 & 11). This is  
475 interpreted to be an active ATF, as it shows similar characteristics to other ATF structures observed in  
476 different localities across the Andes. Namely, they are WNW-trending, are discrete, blind, basement  
477 structures, and show spatial proximity to volcanoes, which can be emplaced at the intersection of the  
478 ATF and arc-parallel fault systems (Cembrano and Lara, 2009; Chernicoff et al., 2002; Lara et al., 2004;  
479 Roquer et al., 2017; Sielfeld et al., 2017; Stanton-Yonge et al., 2016; Veloso et al., 2019; Wrage et al.,  
480 2017). The majority of this WNW seismicity is located below 4 km, suggesting that the fault is located  
481 within the pre-Jurassic basement (Pavez et al., 2016). Furthermore, the seismicity is restricted to the  
482 footwall of the EFS (Figure 6a and Figure 7, WNW-1). The primary correlation is therefore that the  
483 ATF separating the conductive anomalies is seismogenic (e.g., cluster 1 and 2).

484  
485 The seismic cluster Cls2 also occurs at a boundary between a conductive anomaly C4 and the more  
486 resistive region extending NE of the Planchón-Peteroa Volcanic Complex. The most south-eastern  
487 cross-sections, NE-5 & NE-6 (Figure 6), show the progressive disappearance of these features.  
488 Conductors C1 and C2 begin to diminish in strength towards the SW, and seismic clusters dissipate in  
489 NE-5, until there is little distinguishable conductive or seismogenic structure in NE-6. This may be a  
490 result of the model region extending outside the seismic and MT array. The seismic cluster Cls2 is  
491 predominantly focused at 6 – 8 km depth in a region of low to intermediate resistivity (10 - 50  $\Omega\text{m}$ , C4  
492 in Figure 6D-E, sensitivity test 18). The shape of this cluster is very similar to that of the contour of the  
493 conductive anomaly, suggesting a connection between the two (Figure 6D). Furthermore, all seismic  
494 hypocenters occur within a 0-9 km depth range (see Figures 6 & 7).

495  
496 The conductor C1, that extends NW of the Planchón-Peteroa Volcanic Complex, increases in  
497 conductivity northwards from 75  $\Omega\text{m}$  (yellow) until it reaches a maximum of 5  $\Omega\text{m}$  (red) at the  
498 conductive boundary between C1 and R1 (Figure 8B-C, sensitivity test 13). This conductor is also  
499 contained between 4 – 8 km depth, above which there is a low conductivity cap (Figure 7, NE-4,  
500 sensitivity test 3).

501  
502 Figure 6 shows a south to north increase in high conductivity anomalies between 8 – 12 km of depth  
503 (Figure 6 E& F, sensitivity tests 12 & 13), and an apparent connection between C2 and C3 at a 12 km  
504 depth (Figure 6E & F). A smaller conductor, C2 (conductivity ranges 5 - 50 $\Omega\text{m}$ ), is present at a 4 km

505 depth (sensitivity test 15), and connects to a deeper conductor, C3, at 10 km depth along an  
506 approximate north-eastern dip. As MT has difficulty resolving the exact dip of the conductive  
507 anomalies, unless a very dense and localized survey is conducted, this dip angle can only be estimated.  
508 The conductor C3 is also connected through minor conductive branches with the shallow conductor  
509 correlated with the Termas del Flaco geothermal spring (NE-1, NE-2, NW-1 and NW-2, Figure 6), a  
510 known outflow spring of the Tinguiririca geothermal fields (Aravena et al., 2016; Benavente et al.,  
511 2016; Pavez et al., 2016). We interpret this to be the limb of an active hydrothermal system, sourced  
512 from a deeper magmatic body located beneath the Tinguiririca volcanic complex (C3).  
513



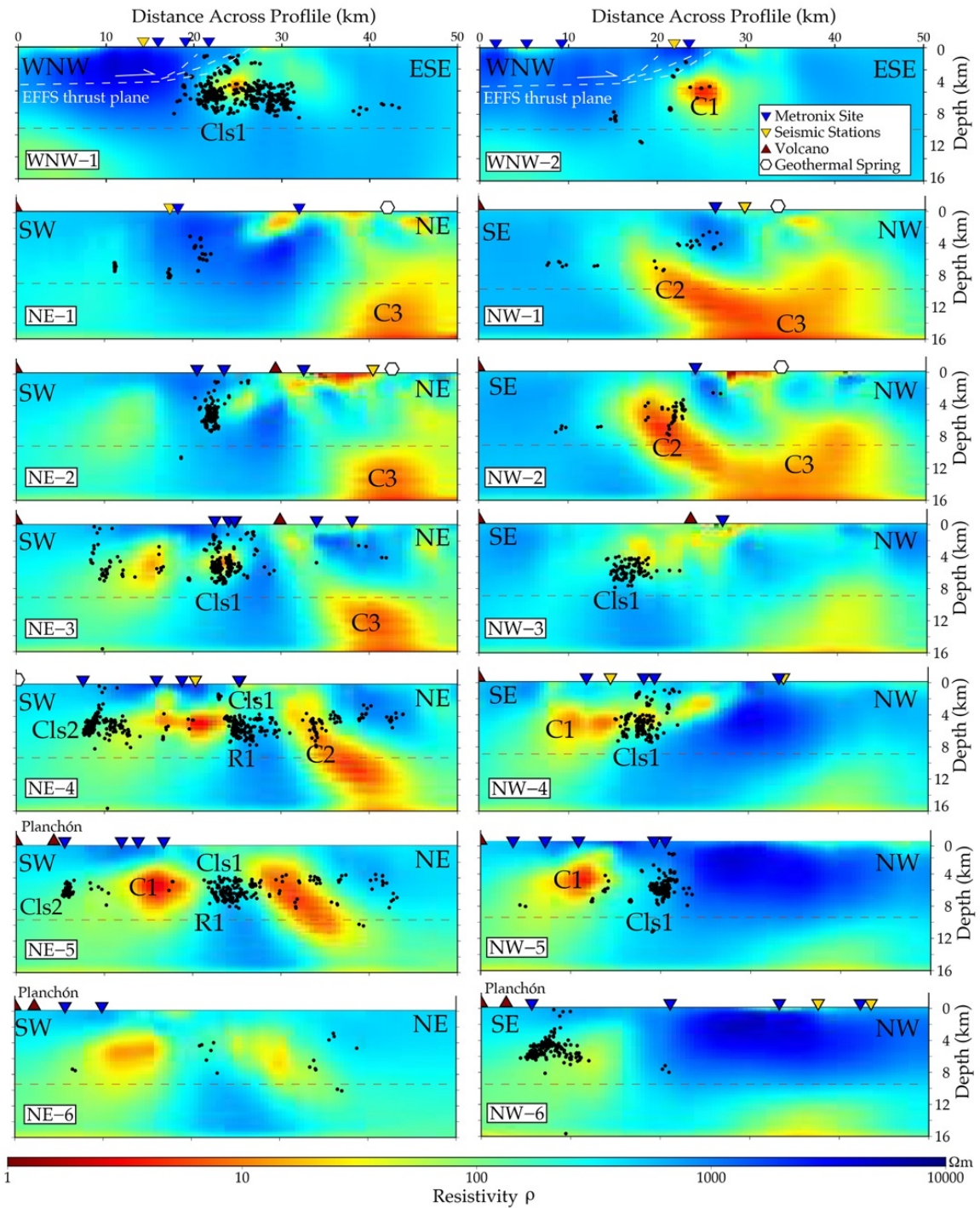
514

515 *Figure 6. A) Hypocenters located from the local seismic survey, projected onto a 12 m resolution DEM*  
 516 *of the field study area along with important geological features (see Figure 2 for feature references).*

517 *B-F: 3D MT models plotted with seismic hypocentres at 2, 4, 6, 8, and 12km depths respectively, with*  
 518 *seismicity projected within ±200m at each depth. The EFFS, volcanoes, and geothermal springs are*

519 *projected onto each map to indicate their surface localities. A-F: White dashed lines indicate the*  
 520 *location of the cross-sections provided in Figure 7.*

521



522

523 *Figure 7. A set of fourteen cross-sections of the MT inversion model between 0 – 16 km, with seismic*  
 524 *hypocenters projected within +/-200 m lateral distance from the transect location. Also projected are*  
 525 *MT and seismic station locations (blue and red triangles respectively) that occur along the transects.*  
 526 *See Figure 6 for profile locations. Conductive and seismic features described in the paper (C1, C2, C3,*  
 527 *R1, Cls1 & Cls2) are labelled. Red dotted line at 9 km marks the depth boundary for seismic activity.*

528

529 In summary, seismic and conductive anomalies appear correlated in Figures 6 and 7. Both high  
530 conductivity anomalies and seismogenic zones occur east of the NNE oriented trend of the volcanic  
531 complexes and EFFS. There is also a prominent WNW oriented seismic cluster, Cls1, that occurs along  
532 an abrupt conductivity boundary (C1 and R1) of the same orientation that emerges at a 4 km depth  
533 and is strongest at a 6 km depth. Below 8 km, the region is aseismic, and a deeply rooted conductor  
534 (C3) emerges beneath the Tinguiririca complex at a 12 km depth that is connected to a smaller  
535 conductive limb that shallows towards the south (C2). Finally, a small seismic cluster (Cls2) shows  
536 coherent geometry and locality with a moderate conductor (C4) at 6-8 km of depth, slightly northwest  
537 of the Planchón-Peteroa edifices.

538

## 539 6 Discussion

540

541 Our results demonstrate that high conductivity zones are located along the axis of the active volcanic  
542 chain (Figure 6B-E). This suggests that the conductors are likely reservoirs of fluid and/or melt related  
543 to the active volcanic arc. As mentioned in section 3, the Andean volcanic arc has an anomalously high  
544 geothermal gradient and high concentrations of magmatically sourced fluids (Benavente et al., 2016;  
545 Giambiagi et al., 2019), both characteristics of which are associated with high conductivity (Ramos,  
546 2010; Turienzo et al., 2012). This correlation of conductive anomalies located along the axis of the  
547 volcanic zone are observed in multiple comparable MT studies conducted in the Southern and Central  
548 Andes (e.g. Díaz et al., 2015; Held et al., 2016; Kapinos et al., 2016). While we have confidence in the  
549 spatial distribution of the conductors in the final MT model, there is some ambiguity as to the absolute  
550 conductivities of each feature. When a precise range of resistivity values for MT anomalies is defined,  
551 lithological properties of subsurface melt and crystalline mush in the Andean volcanic-arc setting can  
552 be resolved (Pommier, 2014), such as melt-fluid fractions (e.g. Cordell et al., 2018; Díaz et al., 2015)  
553 or melt viscosity and silica content (e.g. Comeau et al., 2016b). However, this analysis is best  
554 conducted if specific resistivity values as well as local rheological properties (e.g. melt composition)  
555 are well constrained, and isothermal profiles or the depth extent of hydrothermal fluid circulation  
556 domains are known. Due to the lack of these constraints local to the studied field area, resolving the  
557 lithological properties of conductive phases is not addressed in this study. Interpretation of the  
558 integrated seismic hypocenters and MT model are thus focussed on discerning between melt or  
559 hydrothermal fluids, and their relationship to the seismic features that have been detected.

560

561 The east-west conductivity contrast that is bound by the EFFF fault is particularly apparent in cross-  
562 sections WNW-1 and WNW-2 (Figure 7), on which the dip of the El Fierro fault plane has been  
563 projected using structural data from previous studies of this fault system (Giambiagi et al., 2019;  
564 Godoy et al., 1999). The WNW aligned seismicity cluster Cls1 and conductive anomaly C1 are  
565 contained within the footwall and east of the EFFF, while the domain west of the EFFF is relatively  
566 aseismic. We hypothesize that the EFFF plays a key role in compartmentalising hydrothermal fluids to  
567 the east, as the fault zone acts as a barrier to cross-fault fluid migration, and channels fault-parallel  
568 fluid flow to the surface from depth. This fault structure therefore controls magmatic-derived  
569 hydrothermal fluid circulation and potentially associated seismogenic processes that occur east of the  
570 fault trace. This is supported by the exhumed alteration zone that occurs on the footwall of the  
571 exposed fault surface expression (Figures 3B and 4), and how all geothermal springs and fumaroles  
572 are found along eastern strands of the fault system. The results from Pavez et al. (2016)-(see section  
573 3.3) indicate that the footwall of the EFFF facilitates the circulation of fluids sourced from an andesitic  
574 magma system below 6 km that underlies an active hydrothermal zone. Our data is consistent with  
575 this model, and conductors such as C2 and C3 likely represent such conduits. Furthermore, we believe  
576 that elevated pressures from these fluids may play a role in fault reactivation, as discussed in section  
577 6.4.

578

## 579 6.1 Depth extent of seismicity and the brittle-ductile transition

580

581 The majority of the earthquake hypocentres are located at a depth of 4-6 km, with more shallow  
582 events occurring closer to the EFFF. This suggests that the majority of seismicity is hosted within the  
583 pre-Jurassic basement rocks, and the upper extent of seismicity is delineated by 4-5 km of thick Early  
584 Jurassic-Oligocene rocks (Pavez et al., 2016). At greater depths, there is a distinct seismicity boundary  
585 at around 9 km, below which little seismicity is apparent in any cross-section. Such a seismicity  
586 boundary was observed in the regional scale seismic survey conducted by Sielfeld et al. (2019)  
587 between latitudes 38 - 40°S. Their results show an upper-crustal concave upward seismicity boundary  
588 that traverses the Andes. This boundary is considered concave as the seismic depth limit is 40 km at  
589 the plate margin, 20 km at the back-arc in Argentina, and 10-12 km depth in the Principal Cordillera  
590 that is located between the margin and forearc (Lange et al., 2008; Legrand et al., 2011). It was  
591 suggested by Sielfeld et al. (2019) that this seismicity boundary marks an approximate isotherm of  
592 340°C, based on preceding globally distributed borehole studies of quasi-plastic deformation in the  
593 crust (Suzuki et al., 2014), and the seismicity boundary delineates the brittle-ductile transition zone  
594 within the SVZ. The same interpretation of the seismicity boundary used by Sielfeld et al. (2019) and

595 other comparable MT studies conducted in the southern Andes (e.g. Held et al., 2016) will be applied  
596 to the hypocenter results we have observed. We therefore interpret that the local seismicity boundary  
597 at 9-10 km depth in our area likely indicates the location of the brittle-ductile transition zone and  
598 marks an approximate 340°C isotherm.

599

## 600 6.2 Hydrothermal fluids beneath the Planchón-Peteroa Volcano

601

602 The seismic cluster Cls 2 occurs at 4 – 8 km below and to the NW of Planchón-Peteroa (Figure 7, NE-  
603 4, NE-5 & NW-4), and is concurrent with a moderate conductivity anomaly, C4, of 10 – 50  $\Omega$ m, that is  
604 proximal to the major conductor C1. The conductive anomaly C4 is most prominent and shallowest at  
605 approximately 10 km NW of the volcanic complex, and seismicity spreads from the boundary of the  
606 conductors north-west from Planchón-Peteroa. Furthermore, given the low resolution in the MT  
607 model beneath C1, and as this conductor occurs at the edge of the MT array, it is possible that a more  
608 conductive medium occurs below or south of C1 & C4 that is not resolved by the model. With this  
609 ambiguity in mind, the following rationale provides supporting evidence that C1 & C4 are likely  
610 hydrothermal fluids with some deeper magmatic source. The precise location of the magmatic source  
611 of these fluids remains unknown due to the non-robust regions of the model below and south of C1  
612 and C4.

613

614 The source of C1 and C4 conductivity anomalies is interpreted to be the presence of fluids rather than  
615 magma or crystalline mush, based on previous studies of the Planchón- Peteroa volcanic activity that  
616 have occurred since 2011. It was determined by Aguilera et al. (2016) that the main phreatic eruption  
617 episode was driven by the release of deep magmatic gases as well as volatiles from a shallow  
618 hydrothermal reservoir. Tephra fall and vapour emissions contained no juvenile magmatic  
619 constituents and was mainly of hydrothermal origin. These volcanic products did, however, bear  
620 traces of deep oxidized magmatic fluids from a highly degassed (old) magmatic body, likely of dacitic  
621 or basaltic composition (Tassi et al., 2016). The results from the Tassi et al. (2016) study are supported  
622 by Benavente et al. (2016) who detected minor He signatures of a deep magmatic body within a  
623 dominantly hydrothermal regime below the volcano. It is therefore likely that the conductivity of C1  
624 is largely sourced from the hydrothermal system attested to by these studies. Furthermore, as the  
625 geothermal regime at depths between 0 – 8 km is colder than 340°C (section 6.1), and as the  
626 hydrothermal systems local to this region are established to be at approximately 250°C (Benavente et  
627 al., 2016), C1 and C4 are within the correct depth and temperature range to source these fluids.

628

629 Finally, an InSAR study conducted by Pritchard et al. (2013) detected the subsidence of the Southern  
630 Andean volcanic arc, including Tinguiririca, after the 2010 Mw 8.8 Maule earthquake. Results showed  
631 that the majority of ground deformation caused by the release of fluids from the subvolcanic  
632 hydrothermal systems does not occur directly beneath the volcanic edifice, but is laterally offset from  
633 the main caldera. Additionally, the main geothermal outflow zone for Tinguiririca occurs at Termas de  
634 Flaco, which is located 15 km south of the main volcanic caldera (Pavez et al., 2016). Both studies  
635 provide supporting evidence that the main fluid reservoirs local to individual volcanoes show lateral  
636 offset at depth from the volcano. This supports our deduction that C1 and C4 are hydrothermal-  
637 magmatic reservoirs that are respectively offset NE and NW of the Planchón-Peteroa edifice.

638

639 Having attributed the conductor C1 to a resource of hydrothermal fluids, a likely explanation that the  
640 seismic cluster, Cls2, is induced by fluid migration or degassing of the volcano rather than the  
641 migration of magmatic material. This interpretation is supported by the recent phreatic eruptions that  
642 have characterized the volcano (section 3.1), the spatial proximity of the fluidized (conductive) zones  
643 proximal to the volcano (C1 and C4), and the evidence provided by Benavente et al. (2016) and Tassi  
644 et al. (2016) that the pluton within Planchón-Peteroa is cool and mature. Distinguishing whether the  
645 cluster is sourced from a redistribution of tectonic stress requires further spatial, temporal and  
646 kinematic analysis of the seismic data. However, as the presence of fluids commonly contribute to  
647 seismogenic processes due to the reduction of effective stress local to the faulted structures (Cox,  
648 2005; Cox, 2016), it is reasonable to expect that fluids are present within this cluster. Therefore, this  
649 seismic cluster is interpreted to be a fluid injection point, where episodic seismic release enhances  
650 fluid migration occurring within the volcano.

651

### 652 6.3 Deeply rooted conductor beneath the Tinguiririca Volcano

653

654 The deeper feature, C3, located SW of the Tinguiririca Volcano that emerges at a 6 km depth is beyond  
655 the lateral boundaries of the MT station deployment. However, as magnetotelluric measurements are  
656 capable of increased lateral coverage with increasing depth, and as this feature and its connectivity to  
657 the conductive feature C2 is shown to be robust within the inversion model (sensitivity tests 12, 13 &  
658 15), interpretation is briefly explored. C3 is located SW of the Tinguiririca volcanic complex and is  
659 spatially associated with geothermal outflow springs at Termas del Flaco (refer to section 2.1)  
660 (Aravena et al., 2016; Clavero et al., 2011; Pavez et al., 2016; Pritchard et al., 2013). Its connectivity to  
661 the conductive limb C2, that emerges at a depth of 2 km, suggests that this shallower conductor is  
662 also a component of the active hydrothermal system that has been detected in this area. As trace

663 elements of magmatic sources have been measured in the fumaroles and outflow springs associated  
664 with the Tinguiririca geothermal fields (Benavente et al., 2016), it is possible that these conductors  
665 are comprised of both magmatic material and hydrothermal fluids.

666

667 Considering the dimensions and shallowness of C2, which extends from 2-12 km depth and has a  
668 volume of approximately  $5\text{km}^3$ , it is unlikely that this conductor consists of magma or crystalline mush,  
669 as a more pronounced volcanic feature would be situated above the conductor (Figure 6C-F), as is  
670 observed in comparable studies based in the Andes (e.g. Comeau et al., 2016a; Cordell et al., 2018).  
671 Similar to Planchón-Peteroa, the temperature of the hydrothermal system is estimated to be  $250^\circ\text{C}$   
672 between 2 – 6 km (Benavente et al., 2016), which suggests that a hydrothermal system is dominant  
673 at this depth range. This is supported by the correlating locality of the alteration zone that outcrops  
674 at the footwall of the El Fierro fault (Figure 2), which occurs directly above the conductor C2 (Figure  
675 6B). This suggests that fluid saturated zones have historically migrated towards the surface at this  
676 locality. It is possible that the C2 anomaly is not generated by hydrothermal fluids, but by the  
677 conductive lithological phases of hydrothermally altered material. This does not conflict with the  
678 interpretation that C2 is an ascending limb of the hydrothermal system, but it implies that this  
679 circulation is extinct.

680

681 The deeper conductor C3 is a valid contender as a magmatic reservoir, considering its depth extent  
682 (8-16 km) and location directly beneath the Tinguiririca volcanic complex (Figure 6E-F). It was  
683 established by Pavez et al. (2016) using  $V_p/V_s$  ratios combined with geochemical analyses of fumarolic  
684 discharges that a magmatic body exists 8 – 12 km beneath the Tinguiririca volcanic edifice, which was  
685 determined to be a major source for fluid upflow zones that manifest between 2 – 6 km beneath the  
686 surface (section 3.3). The modelled MT results support this scenario, therefore it is interpreted that  
687 C2 is the signature of zones of hydrothermal fluids migrating to the surface through brittle lithologies.  
688 This interpretation is supported by  $V_p/V_s$  ratios detected by Pavez et. al (2016), which identified  
689 shallow (0-3 km) Mesozoic sedimentary units (Figure 2b) as being highly fractured, thus acting as a  
690 high-permeability conduit for the migration of fluids from a deeper magma source to the surface. The  
691 conductor C3 is generated by crystalline mush or a magmatic body that is a major source of these  
692 fluids, as well as the geochemical traces of magma that have been detected in the geothermal outflow  
693 features local to this volcano (see section 3.2) (Benavente et al., 2016; Pavez et al., 2016). This model  
694 has also been proposed in other districts of the Andes, where a deep (10 – 14 km) conductor beneath  
695 a volcanic edifice is considered a magma reservoir (Comeau et al., 2016a; Díaz et al., 2015), and is the

696 source for hydrothermal reservoirs that circulate in the shallow crust and generate shallower  
697 conductive anomalies (Díaz et al., 2015).

698

#### 699 6.4 Reactivation of WNW Andean Transverse Faults by hydrothermal fluids

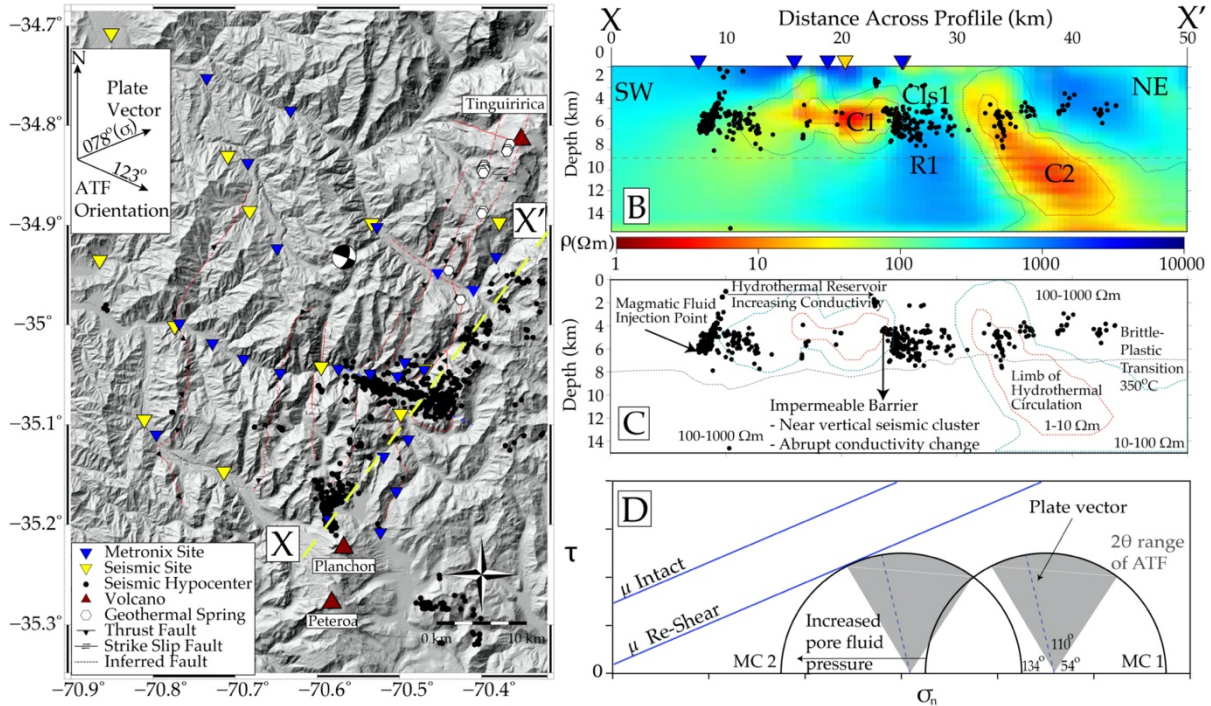
700

701 The WNW-trending cluster of seismicity Cls1 shown in figure 6D is interpreted as an ATF structure  
702 (Figure 8A). As discussed in section 2, these structures are considered discrete, reactivated, pre-  
703 Andean faults, which exert a fundamental control in the location and development of volcanic  
704 features. They are enigmatic as their orientation with respect to the regional stress field makes them  
705 unfavourable to transport magma through the lithosphere (Cembrano and Lara, 2009; Chernicoff et  
706 al., 2002; Piquer et al., 2019; Sielfeld et al., 2019). The seismicity of Cls1 does not extend to the surface,  
707 nor is there any surface expression of the structure, which supports the hypothesis that the ATF  
708 domain is contained within the basement lithology, and that they are of Pre-Andean origin (Cembrano  
709 and Lara, 2009). Recent insights from isotope geochemistry show that the geochemical signatures of  
710 water emerged from ATF have high degrees of crustal contamination (Tardani et al., 2016), signatures  
711 of magmatic vapourization of cold water recharge (Sanchez et al., 2013), and a longer crustal residence  
712 time in the ATF domain relative to major NNE-trending fault systems (Wrage et al., 2017). Structural  
713 and mineralogical analyses of the faults have shown that fluid pressures between >85 - 98% of  
714 lithostatic stress can be required to trigger hybrid (extension plus shear) mode of failure (Roquer et  
715 al. 2017). It is therefore likely that fluid migration through these systems occurs in moments of seismic  
716 activity, and conversely host hydrothermal reservoirs due to the entrapment of fluids during  
717 interseismic periods (Roquer et al., 2017; Veloso et al., 2019). Finally, rare outcrops of the ATF are  
718 characterized by multiple fault cores and dense vein networks within a wide damage zone, which  
719 prevent cross-fault fluid flow due to their low permeability (Lara et al., 2004; Perez-Flores et al., 2016)

720

721 The seismic cluster Cls1 follows the distinct conductivity contrast of the conductor C1 and resistor R1  
722 (see section 5.2). The occurrence of seismogenic features at abrupt conductive boundaries has been  
723 observed in comparable MT and seismic studies conducted along the San Andreas Fault, Taupo  
724 Volcanic Zone and an intraplate setting in central Botswana (Becken et al., 2011; Ingham et al., 2009;  
725 Moorkamp et al., 2010). These studies suggest that earthquakes tend to occur adjacent to zones of  
726 high conductivity, either at the boundaries or within the regions of the neighbouring resistive rock.  
727 This occurrence is due to the migration of fluids into a permeable, mechanically weak zone  
728 (characterized by low resistivity) adjacent to a less permeable, mechanically strong zone  
729 (characterized by high resistivity), causing the accumulation of high fluid pressures and subsequent  
730 brittle rock failure (Becken et al., 2011; Cox, 2005). This process can occur in fault zones, where

731 impermeable fault cores prevent cross-fault fluid flow causing the increase of local fluid pressures,  
 732 while the permeable fracture mesh aligned parallel to the fault core enhances fault-parallel fluid flow  
 733 (Faulkner et al., 2010; Hoffman-Rothe et al., 2004; Rowland and Sibson, 2004; Sibson, 1996).  
 734



735  
 736 *Figure 8. All relative relocated seismic hypocenters from the local seismic survey, projected onto a the*  
 737 *12.5m resolution DEM of the field study area. The Teno earthquake moment tensor (Ekstrom et al.,*  
 738 *2012), geothermal springs, Holocene volcano locations and associated units, station locations and El*  
 739 *Fierro Fault System are also shown. B) NE-oriented cross-section of the MT model with seismic*  
 740 *hypocenters projected within a 200m lateral range of the cross section location; C) Schematic*  
 741 *interpretation of the cross-section in panel B. D) a theoretical Mohr circle diagram illustrating the*  
 742 *failure criterion envelopes for different stress regimes for fault re-shear, and the effect of pore fluid*  
 743 *pressures on equivalent stress scenarios, each circle is marked as MC1 - 2. Greyed area represents*  
 744 *range of quaternary stress orientations from Giambiagi et al. (2019)*

745

746 The predominance of seismicity at abrupt conductivity contrasts suggests that fluid accumulation can  
 747 locally trigger reactivation of pre-existing ATF structures. It is interpreted that the smaller seismic  
 748 cluster that resides beneath the Planchón-Peteroa system (CIs2) is a channel for volcanically sourced  
 749 fluids that accumulate in a hydrothermal reservoir north of the complex. This reservoir is the source  
 750 of the anomaly C1, which increases in conductivity northwards until it reaches a maximum at the  
 751 conductive boundary between C1 and R1, and the seismic cloud, CIs1. We illustrate the state of stress  
 752 using a Mohr-Coulomb failure diagram (Figure 8D), which is drawn on the assumption that the ATF

753 are inherent, WNW-oriented, pre-Andean structures with a strike of approximately 110° (estimated  
754 from the 2004 Mw 6.5 Teno earthquake focal mechanism (Ekstrom et al., 2012)), with no cohesive  
755 strength (Sibson, 1985). These faults activate as sinistral-strike slip and reverse modes under the  
756 current stress regime (Stanton-Yonge et al., 2016), evident from the 2004 Mw 6.5 focal mechanism  
757 (Figure 9A) and observations from similar ATF structures south of the studied area (Sielfeld et al.,  
758 2019). A simple Andersonian relationship is assumed (Anderson, 1942), where  $\sigma_2$  is along the vertical  
759 axis and  $\sigma_1$  and  $\sigma_3$  are in a horizontal plane, and that  $\sigma_1$  ranges between N65°E to N88°E, considering  
760 the angle of convergence and the associated possible orientations of the instantaneous shortening  
761 axes in a transpressional margin (Perez-Flores et al., 2016; Teyssier et al., 1995). The angle between  
762  $\sigma_1$  and the fault plane is approximately between 58° to 35°, showing that it is not optimally oriented  
763 for reactivation. Therefore, increasing fluid pressure could induce reactivation of the fault by  
764 decreasing the effective normal stress. In the absence of local measurements of stress orientations,  
765 there is uncertainty as to whether the stress field includes strain partitioning across the  
766 transpressional plate margin (e.g. Teyssier et al., 1995; Tikoff and Teyssier, 1994) and/or mechanical  
767 interaction between faults across the volcanic arc (e.g. Stanton-Yonge et al., 2016). Future studies will  
768 be conducted using our seismic catalogue to determine fault plane solutions and conduct a kinematic  
769 analysis of fault-slip data, and thus constrain local stress orientations.

770

771 It should be noted that a small protrusion of C1 occurs at 4 km depth above Cls1, observable in Figure  
772 6C and cross-sections NW-3 and NW-4. This conductor may represent fluid migration, however as it  
773 does not cross the seismic cluster region, we regard this feature to support our argument that the  
774 observed ATF is impermeable to fluid flow.

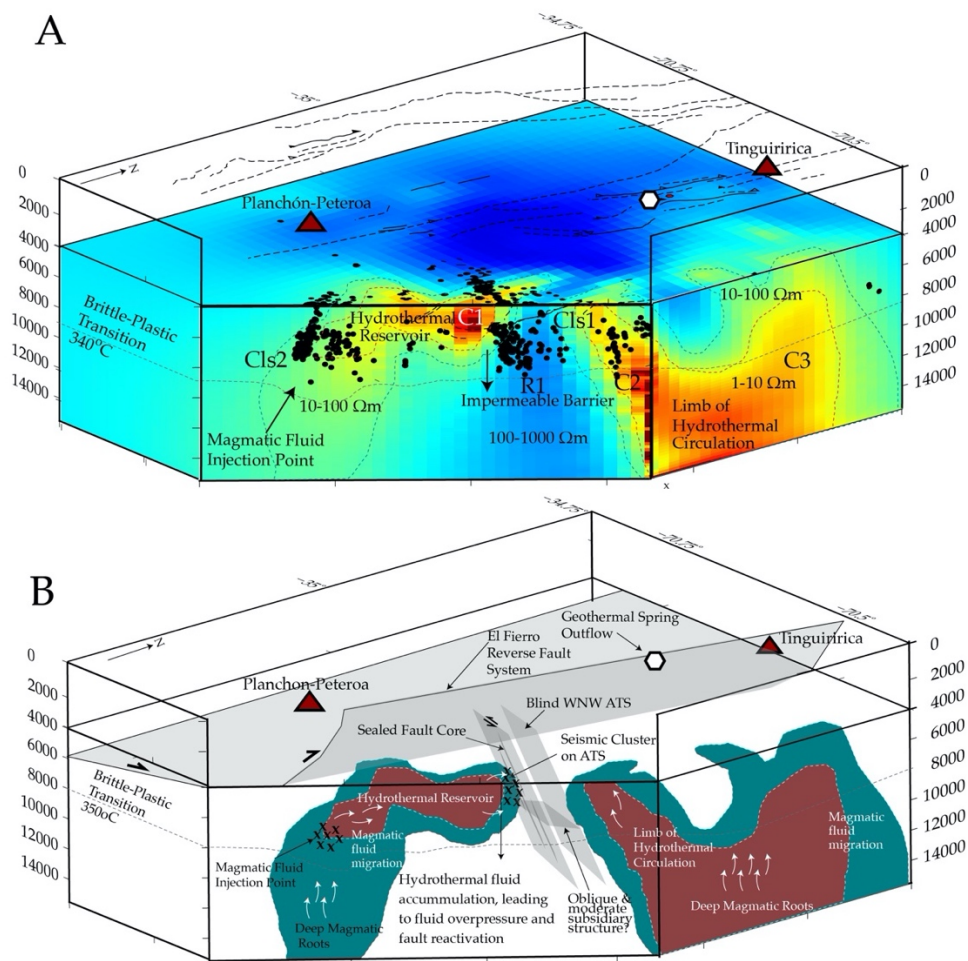
775

## 776 6.5 Conceptual model of hydrothermal system

777

778 Figure 9A shows a 3D representation of the final model. It is interpreted that the resistive, seismogenic  
779 structure considered to be an ATF interacts with the deeply rooted conductor beneath Tinguiririca.  
780 We interpret the conductor C2 to be the limb of a hydrothermal system sourced from a magmatic  
781 origin identified with the deeper conductor, C3 (section 6.3). This limb channels fluids towards the  
782 surface along the fault plane of the ATF. Unlike the hydrothermal reservoir on the southern region  
783 (C1), which results in overpressure and drives fault reactivation (section 6), the region surrounding  
784 the conductor C2 shows no dense seismic clusters. We suggest that the conductor C2 is a zone of  
785 permeable, saturated rock within which the pore fluid pressure is in excess of hydrostatic pressure.  
786 This hypothesis is supported by the presence of significant geothermal outflow springs of deep-  
787 sourced fluids, such as those found at Termas del Flaco, which accumulate in the geothermal fields

788 associated with the Tinguiririca volcanic complex (Aravena et al., 2016; Benavente et al., 2016;  
 789 Giambiagi et al., 2019; Pavez et al., 2016; Pritchard et al., 2013). Conversely, the Planchón-Peteroa  
 790 reservoir has a resistive cap that extends to 4 km depth. The presence of capping structures in the ATF  
 791 domain have been previously hypothesized as a control on their rupture cycle (Roquer et al., 2017).  
 792 The conductor C1 is therefore contained at depth of 4 km by the resistive cap, is northwardly bound  
 793 by the ATF of a WNW orientation, and is westward bound by the EFS of a NNE-orientation. The  
 794 conductor therefore occurs at the intersection of these two fault structures.  
 795



796  
 797 *Figure 9. A) 3D presentation of the conductivity model at 4km depth along the horizontal plane, and*  
 798 *cross-sections NE-4 and NW-2 (Figure 7) from 4-16km depth placed at accurate transect locations.*  
 799 *Seismic hypocenters are shown along these planes to illustrate their distribution in 3D, with all*  
 800 *seismicity projected onto the 4km horizontal plane to highlight the NW orientation of Cls. 1.*  
 801 *Annotations highlight the interpretations discussed in sections 5 - 7, and the EFS and volcanic*  
 802 *complexes are projected at 0km depth to contextualize their locality at the surface; B) A schematic*  
 803 *interpretation of the model results illustrates the hydro-volcanic system that is proposed for this area*  
 804 *(Section 7)*

805

806 This tectono-hydrothermal environment has been observed in different regions of the Andes that the  
807 intersection of major NNE thrust faults and ATF are hosts to giant ore-porphyry deposits (Figure 1)  
808 (e.g. Chernicoff et al., 2002; Cox, 2005; Curewitz and Karson, 1997; Piquer et al., 2019; Rowland and  
809 Simmons, 2012; Sillitoe, 1997; Veloso et al., 2019). These points of intersection have also been  
810 deduced to impact geothermal reservoir development (Perez-Flores et al., 2017; Sanchez et al., 2013).  
811 Therefore, this study provides a site specific example of how the intersection of these major, margin-  
812 parallel thrust fault systems and Andean transverse faults are hosts to magmatically sourced  
813 hydrothermal reservoirs at 4 – 8 km depths.

814

815

## 816 7 Conclusions

817

818 Results from this combined magnetotelluric and seismic study can be summarized with five distinct  
819 observations:

820

821 1. An eastern conductive and western resistive domain is correlated with a seismicity boundary that  
822 occurs across all depths, following the trend of the volcanic arc and NNE-trending El Fierro Fault  
823 system. This is interpreted to be the signature of magmatic sources beneath the volcanic arc. These  
824 domains are characterized by higher conductivities than the surrounding regions due to high  
825 temperatures and the concentration of volcanically derived fluids. We also conclude that these  
826 conductive and seismic signatures are bounded by the footwall of the El Fierro fault system, due to  
827 the low permeability fault cores that prevent cross-fault fluid migration.

828

829 2. A WNW-trending seismogenic fault is identified on an abrupt electrical conductivity contrast that  
830 occurs between 4 - 8km of depth. We interpret this seismogenic feature to be a reactivated Andean  
831 Transverse Fault (ATF), and the electrically conductive domain to be a hydrothermal reservoir. We  
832 conclude that the impermeable fault core of the ATF prevents cross-fault fluid flow, therefore, the  
833 accumulation of fluids increases pore fluid pressures and favours fault reactivation despite its  
834 unfavourable orientation relative to the regional stress field.

835

836 3. A deep conductor beneath the Tinguiririca volcanic complex emerges at an 8 km depth and  
837 increases in volume and conductivity with increasing depth. It shows some connection to the surface

838 with minor conductive branches that show spatial coherence with the major geothermal outflow  
839 spring Termas del Flaco. This high conductivity anomaly is interpreted to be a deep volcanic root that  
840 sources the geothermal springs and fumaroles observed at the base and edifice of the Tinguiririca  
841 volcanic complex, as well as the geothermal fields that have been thoroughly prospected in this area.

842

843 4. There is a minor seismic cluster and conductor beneath the Planchón-Peteroa volcanic complex that  
844 is highly concentrated at 8 km depths. These volcanoes have been intermittently on yellow- alert for  
845 ash emission and degassing events since 2011 suggesting this seismicity is related to the release of  
846 volcanic derived fluids and volatiles into the shallower crust, recharging the hydrothermal reservoir  
847 above.

848

849 5. There is a distinct aseismic boundary at 8-10 km of depth, below which there is no seismicity. This  
850 is interpreted to be the brittle-ductile transition zone, and a definitive 340°C isotherm that is observed  
851 across the Andean volcanic margin.

852

853 6. The hydrothermal reservoir that extends NW from the Planchón-Peteroa volcano is contained at  
854 the intersection of the NNE-trending EFFS, the WNW-trending ATF, and a resistive cap that extends to  
855 a depth of 4 km. These results support preceding evidence that hydrothermal reservoirs and ore  
856 deposits occur at intersections of these fault systems at multiple locations across the Andes.

857

858 This combined seismic and magnetotelluric study provides a site-specific example of how an ATF  
859 interacts with local volcanic and hydrothermal systems. In this case, it is proposed that the ATF fails  
860 despite its non-optimal orientation with respect to the regional stress field due to the influence of  
861 pore fluid pressures acting on the fault plane. These results contribute to our understanding of the  
862 mechanical and architectural relationship of the ATF and NNE-trending, margin parallel fault systems,  
863 and their control on the spatial development of hydrothermal reservoirs. These conclusions may be  
864 applicable to other occurrences of intersecting ATF and NNE-trending fault systems in the Andean  
865 Southern Volcanic Zone.

866

## 867 Acknowledgments

868

869 Funding was provided by NERC grant NE/M004716/1 to TMM and an RTSG to RKP and ASMG from  
870 the London NERC DTP, with financial help from the Chilean National Fund for Scientific and  
871 Technological Development (FONDECYT: grant number 1141139), and the Canadian Centennial

872 Scholarship Fund (CCSF), to whom we express our sincerest gratitude for making the study possible.  
873 We are very grateful to all of those involved in the field work, through the allotment of land to  
874 deploy our instruments, and the assistance in the logistics and/or labour of the deployment. For  
875 their incredible contribution to this effort, we would like to give special thanks to Mariel Castillo,  
876 Matias Cavieres, Manuel Dorr, Victorino Arauco, Gerd Seilfeld, Elias Lira, Nati & Mati Mohring, Jac  
877 Thomas, Emily Franklin, Pamela Prez-Flores, James Strachan, Daniela Balladares, Steve Boon, John  
878 Browning, Ronny Figueroa and Javiera Ruz. Broadband magnetotelluric equipment was kindly  
879 provided by PUC and Universidad de Chile. All MT transfer functions are publicly available on the IRIS  
880 EMTF archive (Kelbert et al., 2011), listed under doi:10.17611/DP/EMTF/UCL/CHILEMT. Many thanks  
881 to Anna Kelbert for her support during the archival process, and to Jared Peacock for his assistance  
882 in the use of MTPy (Peacock et al., 2019). The UK seismic instruments and data management  
883 facilities were provided under loan number 1073 by SEIS-UK at the University of Leicester. The  
884 facilities of SEIS-UK are supported by the NERC under Agreement R8/H10/64. All seismic data are  
885 archived at IRIS ([https://www.fdsn.org/networks/detail/6A\\_2017/](https://www.fdsn.org/networks/detail/6A_2017/)). QuakeMigrate software is  
886 hosted in GitHub platform (<https://github.com/QuakeMigrate/QuakeMigrate>).  
887

888  
889

## 890 References

891  
892

- 893 Acocella, V., Gioncada, A., Omarini, R., Riller, U., Mazzuoli, R., Vezzoli, L., 2011. Tectonomagmatic  
894 characteristics of the back-arc portion of the Calama-Olacapato-El Toro Fault Zone, Central Andes.  
895 *Tectonics* 30.
- 896 Aguilera, F., Benavente, Ó., Gutiérrez, F., Romero, J., Saltori, O., González, R., Agosto, M., Caselli, A.,  
897 Pizarro, M., 2016. Eruptive activity of planchón-peteroa volcano for period 2010-2011, southern  
898 andean volcanic zone, chile. *Andean Geology* 43, 20-46.
- 899 Anderson, E.M., 1942. The dynamics of faulting and dyke formation with applications to Britain. Oliver  
900 and Boyd, Edinburgh, 191pp.
- 901 Angermann, D., Klotz, J., Reigber, C., 1999. Space-geodetic estimation of the Nazca-South America  
902 Euler vector. *Earth and Planetary Science Letters* 171, 329-334.
- 903 Aravena, D., Munoz, M., Morata, D., Lahsen, A., Parada, M.A., Dobson, P., 2016. Assessment of high  
904 enthalpy geothermal resources and promising areas of Chile. *Geothermics* 59, 1-13.
- 905 Aron, F., Cembrano, J., Astudillo, F., Allmendinger, R.W., Arancibia, G., 2015. Constructing forearc  
906 architecture over megathrust seismic cycles: Geological snapshots from the Maule earthquake region,  
907 Chile. *Geological Society of America Bulletin* 127, 464-479.
- 908 Avdeev, D., Avdeeva, A., 2009. 3D magnetotelluric inversion using a limited-memory quasi-Newton  
909 optimization. *Geophysics* 74, F45-F57.
- 910 Avdeev, D.B., 2005. Three-dimensional electromagnetic modelling and inversion from theory to  
911 application. *Surv Geophys* 26, 767-799.
- 912 Becken, M., Ritter, O., 2012. Magnetotelluric Studies at the San Andreas Fault Zone: Implications for  
913 the Role of Fluids. *Surv Geophys* 33, 65-105.
- 914 Becken, M., Ritter, O., Bedrosian, P.A., Weckmann, U., 2011. Correlation between deep fluids, tremor  
915 and creep along the central San Andreas fault. *Nature* 480, 87-U248.
- 916 Benavente, O., Tassi, F., Reich, M., Aguilera, F., Capecchiacci, F., Gutierrez, F., Vaselli, O., Rizzo, A.,  
917 2016. Chemical and isotopic features of cold and thermal fluids discharged in the Southern Volcanic

- 918 Zone between 32.5 degrees S and 36 degrees S: Insights into the physical and chemical processes  
919 controlling fluid geochemistry in geothermal systems of Central Chile. *Chemical Geology* 420, 97-113.
- 920 Bertrand, E., Caldwell, T., Hill, G., Wallin, E., Bennie, S., Cozens, N., Onacha, S., Ryan, G., Walter, C.,  
921 Zaino, A., 2012. Magnetotelluric imaging of upper-crustal convection plumes beneath the Taupo  
922 Volcanic Zone, New Zealand. *Geophysical Research Letters* 39.
- 923 Bibby, H., Caldwell, T., Brown, C., 2005. Determinable and non-determinable parameters of galvanic  
924 distortion in magnetotellurics. *Geophysical Journal International* 163, 915-930.
- 925 Bonali, F.L., Tibaldi, A., Corazzato, C., Tormey, D.R., Lara, L.E., 2013. Quantifying the effect of large  
926 earthquakes in promoting eruptions due to stress changes on magma pathway: The Chile case.  
927 *Tectonophysics* 583, 54-67.
- 928 Caine, J.S., Evans, J.P., Forster, C.B., 1996. Fault zone architecture and permeability structure. *Geology*  
929 24, 1025-1028.
- 930 Cembrano, J., Lara, L., 2009. The link between volcanism and tectonics in the southern volcanic zone  
931 of the Chilean Andes: A review. *Tectonophysics* 471, 96-113.
- 932 Charrier, R., Baeza, O., Elgueta, S., Flynn, J.J., Gans, P., Kay, S.M., Munoz, N., Wyss, A.R., Zurita, E.,  
933 2002. Evidence for Cenozoic extensional basin development and tectonic inversion south of the flat-  
934 slab segment, southern Central Andes, Chile (33 degrees-36 degrees SL). *Journal of South American*  
935 *Earth Sciences* 15, 117-139.
- 936 Charrier, R., Pinto, L., Rodríguez, M.P., 2007. Tectonostratigraphic evolution of the Andean Orogen in  
937 Chile, Geological Society Special Publication, pp. 21-114.
- 938 Charrier, R., Ramos, V.A., Tapia, F., Sagripanti, L., 2015. Tectono-stratigraphic evolution of the Andean  
939 Orogen between 31 and 37°S (Chile and Western Argentina). Geological Society, London, Special  
940 Publications 399, 13-61.
- 941 Chave, A.D., 1989. BIRRP: Bounded Influence, Remote Reference Processing. *J. Geophys. Res* 94,  
942 14215-14225.
- 943 Chave, A.D., Thomson, D.J., 2003. A bounded influence regression estimator based on the statistics of  
944 the hat matrix. *J R Stat Soc C-Appl* 52, 307-322.
- 945 Chernicoff, C.J., Richards, J.P., Zappettini, E.O., 2002. Crustal lineament control on magmatism and  
946 mineralization in northwestern Argentina: geological, geophysical, and remote sensing evidence. *Ore*  
947 *Geology Reviews* 21, 127-155.
- 948 Clavero, J., Pineda, G., Mayorga, C., Giavelli, A., Aguirre, I., Simmons, S., Martini, S., Soffia, J., Arriaza,  
949 R., Polanco, E., 2011. Geological, geochemical, geophysical and first drilling data from Tinguiririca  
950 geothermal area, central Chile. *Geothermal Resources Council Transactions* 35, 731-734.
- 951 Comeau, M.J., Unsworth, M.J., Cordell, D., 2016a. New constraints on the magma distribution and  
952 composition beneath Volcan Uturuncu and the southern Bolivian Altiplano from magnetotelluric data.  
953 *Geosphere* 12, 1391-1421.
- 954 Comeau, M.J., Unsworth, M.J., Cordell, D., 2016b. New constraints on the magma distribution and  
955 composition beneath Volcán Uturuncu and the southern Bolivian Altiplano from magnetotelluric data.  
956 *Geosphere* 12, 1391-1421.
- 957 Cordell, D., Unsworth, M.J., Díaz, D., 2018. Imaging the Laguna del Maule Volcanic Field, central Chile  
958 using magnetotellurics: Evidence for crustal melt regions laterally-offset from surface vents and lava  
959 flows. *Earth and Planetary Science Letters* 488, 168-180.
- 960 Cox, S.F., 2005. Coupling between deformation, fluid pressures, and fluid flow in ore-producing  
961 hydrothermal systems at depth in the crust. *Economic Geology* 100, 39-75.
- 962 Cox, S.F., 2010. The application of failure mode diagrams for exploring the roles of fluid pressure and  
963 stress states in controlling styles of fracture-controlled permeability enhancement in faults and shear  
964 zones. *Geofluids* 10, 217-233.
- 965 Cox, S.F., 2016. Injection-Driven Swarm Seismicity and Permeability Enhancement: Implications for  
966 the Dynamics of Hydrothermal Ore Systems in High Fluid-Flux, Overpressured Faulting Regimes-An  
967 Invited Paper. *Economic Geology* 111, 559-587.

- 968 Curewitz, D., Karson, J.A., 1997. Structural settings of hydrothermal outflow: Fracture permeability  
969 maintained by fault propagation and interaction. *J Volcanol Geoth Res* 79, 149-168.
- 970 Díaz, D., Heise, W., Zamudio, F., 2015. Three-dimensional resistivity image of the magmatic system  
971 beneath Lastarria volcano and evidence for magmatic intrusion in the back arc (northern Chile).  
972 *Geophysical Research Letters* 42, 5212-5218.
- 973 Drew, J., White, R.S., Tilmann, F., Tarasewicz, J., 2013. Coalescence microseismic mapping.  
974 *Geophysical Journal International* 195, 1773-1785.
- 975 Droguett, B., Morata, D., Clavero, J., Pineda, G., Morales-Ruano, S., Carrillo-Rosúa, J., 2012.  
976 *Mineralogía de alteración en el pozo Pte-1, campo geotermal Tinguiririca, Chile.*
- 977 Ekstrom, G., Nettles, M., Dziewonski, A.M., 2012. The global CMT project 2004-2010: Centroid-  
978 moment tensors for 13,017 earthquakes. *Physics of the Earth and Planetary Interiors* 200, 1-9.
- 979 Farias, M., Comte, D., Charrier, R., Martinod, J., David, C., Tassara, A., Tapia, F., Fock, A., 2010. Crustal-  
980 scale structural architecture in central Chile based on seismicity and surface geology: Implications for  
981 Andean mountain building. *Tectonics* 29.
- 982 Faulkner, D.R., Jackson, C.A.L., Lunn, R.J., Schlische, R.W., Shipton, Z.K., Wibberley, C.A.J., Withjack,  
983 M.O., 2010. A review of recent developments concerning the structure, mechanics and fluid flow  
984 properties of fault zones. *Journal of Structural Geology* 32, 1557-1575.
- 985 Giambiagi, L., Alvarez, P., Spagnotto, S., Godoy, E., Lossada, A., Mescua, J., Barrionuevo, M., Suriano,  
986 J., 2019. Geomechanical model for a seismically active geothermal field: Insights from the Tinguiririca  
987 volcanic-hydrothermal system. *Geosci Front* 10, 2117-2133.
- 988 Godoy, E., Lara, L., 1994. Segmentación estructural andina a los 33-34: nuevos datos en la Cordillera  
989 Principal, Congreso Geológico Chileno, pp. 1344-1348.
- 990 Godoy, E., Yanez, G., Vera, E., 1999. Inversion of an Oligocene volcano-tectonic basin and uplifting of  
991 its superimposed Miocene magmatic arc in the Chilean Central Andes: first seismic and gravity  
992 evidences. *Tectonophysics* 306, 217-236.
- 993 Gow, P.A., Walshe, J.L., 2005. The role of preexisting geologic architecture in the formation of giant  
994 porphyry-related Cu +/- Au deposits: Examples from New Guinea and Chile. *Economic Geology* 100,  
995 819-833.
- 996 GVP, 2020. Global Volcanism Program, Smithsonian Institution.
- 997 Hammond, J.O.S., Garzon, A.S.D.L.M., Pearce, R., Marshall, N., Mitchell, T., Cembrano, J., 2017. Teno  
998 Valley Seismic Network [Data set]. International Federation of Digital Seismograph Networks.
- 999 Hedenquist, J.W., Lowenstern, J.B., 1994. The Role of Magmas in the Formation of Hydrothermal Ore-  
1000 Deposits. *Nature* 370, 519-527.
- 1001 Held, S., Schill, E., Pavez, M., Diaz, D., Munoz, G., Morata, D., Kohl, T., 2016. Resistivity distribution  
1002 from mid-crustal conductor to near-surface across the 1200 km long Liquine-Ofqui Fault System,  
1003 southern Chile. *Geophysical Journal International* 207, 1387-1400.
- 1004 Hickson, C., Ferraris, F., Rodriguez, C., Sielfeld, G., Henriquez, R., Gislason, T., Selters, J., Benoit, D.,  
1005 White, P., Southon, J., 2011. The Mariposa Geothermal System, Chile. *Geothermal Resources Council*  
1006 *Transactions* 35, 817-825.
- 1007 Hoffman-Rothe, A., Ritter, O., Janssen, C., 2004. Correlation of electrical conductivity and structural  
1008 damage at a major strike-slip fault in northern Chile. *Journal of Geophysical Research-Solid Earth* 109.
- 1009 Ingham, M.R., Bibby, H.M., Heise, W., Jones, K.A., Cairns, P., Dravitzki, S., Bennie, S.L., Caldwell, T.G.,  
1010 Ogawa, Y., 2009. A magnetotelluric study of Mount Ruapehu volcano, New Zealand. *Geophysical*  
1011 *Journal International* 179, 887-904.
- 1012 Kapinos, G., Montahaei, M., Meqbel, N., Brasse, H., 2016. Three-dimensional electrical resistivity  
1013 image of the South-Central Chilean subduction zone. *Tectonophysics* 666, 76-89.
- 1014 Katz, H., 1971. Continental margin in Chile—is tectonic style compressional or extensional? *AAPG*  
1015 *Bulletin* 55, 1753-1758.
- 1016 Kelbert, A., Egbert, G., Schultz, A., 2011. IRIS DMC data services products: EMTF, the magnetotelluric  
1017 transfer functions. National Geoelectromagnetic Facility Technical Report.

- 1018 Kissling, E., Ellsworth, W.L., Eberhartphillips, D., Kradolfer, U., 1994. Initial Reference Models in Local  
1019 Earthquake Tomography. *Journal of Geophysical Research-Solid Earth* 99, 19635-19646.
- 1020 Klein, F.W., 2002. User's guide to HYPOINVERSE-2000, a Fortran program to solve for earthquake  
1021 locations and magnitudes. US Geological Survey.
- 1022 Lange, D., Cembrano, J., Rietbrock, A., Haberland, C., Dahm, T., Bataille, K., 2008. First seismic record  
1023 for intra-arc strike-slip tectonics along the Liquine-Ofqui fault zone at the obliquely convergent plate  
1024 margin of the southern Andes. *Tectonophysics* 455, 14-24.
- 1025 Lara, L., Naranjo, J., Moreno, H., 2004. Rhyodacitic fissure eruption in Southern Andes (Cordón Caulle;  
1026 40.5 S) after the 1960 (Mw: 9.5) Chilean earthquake: a structural interpretation. *J Volcanol Geoth Res*  
1027 138, 127-138.
- 1028 Lara, L.E., Lavenu, A., Cembrano, J., Rodriguez, C., 2006. Structural controls of volcanism in transversal  
1029 chains: Resheared faults and neotectonics in the Cordon Caulle-Puyehue area (40.5 degrees S),  
1030 Southern Andes. *J Volcanol Geoth Res* 158, 70-86.
- 1031 Legrand, D., Barrientos, S., Bataille, K., Cembrano, J., Pavez, A., 2011. The fluid-driven tectonic swarm  
1032 of Aysen Fjord, Chile (2007) associated with two earthquakes (Mw=6.1 and Mw=6.2) within the  
1033 Liquine-Ofqui Fault Zone. *Cont Shelf Res* 31, 154-161.
- 1034 Lira Martínez, E.S., 2011. Estudio de sismicidad, tomografía sísmica y modelo de física de rocas:  
1035 Potencial sistema geotermal asociado al complejo volcánico Tinguiririca.
- 1036 Melnick, D., Bookhagen, B., Strecker, M.R., Echtler, H.P., 2009. Segmentation of megathrust rupture  
1037 zones from fore-arc deformation patterns over hundreds to millions of years, Arauco peninsula, Chile.  
1038 *Journal of Geophysical Research-Solid Earth* 114.
- 1039 Melnick, D., Echtler, H.P., 2006. Morphotectonic and Geologic Digital Map Compilations of the South-  
1040 Central Andes (36 degrees-42 degrees S). *Front Earth Sci Ser*, 565-568.
- 1041 Mescua, J.F., Giambiagi, L.B., Ramos, V.A., 2013. Late Cretaceous uplift in the Malargüe fold-and-thrust  
1042 belt (35° S), southern Central Andes of Argentina and Chile. *Andean Geology* 40, 102-116.
- 1043 Micklethwaite, S., Sheldon, H.A., Baker, T., 2010. Active fault and shear processes and their  
1044 implications for mineral deposit formation and discovery. *Journal of Structural Geology* 32, 151-165.
- 1045 Miensoopust, M.P., Queralt, P., Jones, A.G., Modellers, D.M., 2013. Magnetotelluric 3-D inversion-a  
1046 review of two successful workshops on forward and inversion code testing and comparison.  
1047 *Geophysical Journal International* 193, 1216-1238.
- 1048 Moorkamp, M., Jones, A.G., Fishwick, S., 2010. Joint inversion of receiver functions, surface wave  
1049 dispersion, and magnetotelluric data. *Journal of Geophysical Research-Solid Earth* 115.
- 1050 Moreno, H., 1976. The Upper Cenozoic Volcanism in the Andes of Southern Chile (From 40 00 'to 41  
1051 30 'SL), *Proc IAVCEI Symposium on Andean and Antarctic Volcanology Problems*, pp. 143-171.
- 1052 Mpodozis, C., Cornejo, P., 2012. Cenozoic Tectonics and Porphyry Copper Systems of the Chilean  
1053 Andes. *Soc Econ Geol Spec P*, 329-360.
- 1054 Mpodozis, C., Ramos, V., Ericksen, G., Canas Pinochet, M., Reinemund, J., 1989. Geology of the Andes  
1055 and its Relation to Hydrocarbon and Mineral Resources, pp. 59-90.
- 1056 Nakamura, K., 1977. Volcanos as Possible Indicators of Tectonic Stress Orientation - Principle and  
1057 Proposal. *J Volcanol Geoth Res* 2, 1-16.
- 1058 Núñez Tapia, R.C., 2018. Procesos de transporte de fluidos hidrotermales a lo largo de un sistema de  
1059 fallas: geología estructural y modelamiento numérico con elementos de borde.
- 1060 Palsar, A., 2011. Jaxa/meti a los palsar. . Alaska Satellite Facility, (ALP- SRP264684320).
- 1061 Pardo, M., Vera, E., Yáñez, G., Monfret, T., 2009. Tomografía sísmica bajo los Andes de Chile Central  
1062 (33-34.5 S): Implicaciones sismotectónicas, *Congreso Geológico Chileno*, pp. S9-067.
- 1063 Pavez, C., Tapia, F., Comte, D., Gutierrez, F., Lira, E., Charrier, R., Benavente, O., 2016. Characterization  
1064 of the hydrothermal system of the Tinguiririca Volcanic Complex, Central Chile, using structural  
1065 geology and passive seismic tomography. *J Volcanol Geoth Res* 310, 107-117.
- 1066 Peacock, J., Kirkby, A.L., Zhang, F., Hassan, R., Duan, J., 2019. MTPy: A Python toolbox for  
1067 magnetotelluric data. *AGUFM 2019, NS21A-06*.

- 1068 Perez-Flores, P., Cembrano, J., Sanchez-Alfaro, P., Veloso, E., Arancibia, G., Roquer, T., 2016. Tectonics,  
1069 magmatism and paleo-fluid distribution in a strike-slip setting: Insights from the northern termination  
1070 of the Liquine-Ofqui fault System, Chile. *Tectonophysics* 680, 192-210.
- 1071 Perez-Flores, P., Veloso, E., Cembrano, J., Sanchez-Alfaro, P., Lizama, M., Arancibia, G., 2017. Fracture  
1072 network, fluid pathways and paleostress at the Tolhuaca geothermal field. *Journal of Structural*  
1073 *Geology* 96, 134-148.
- 1074 Piquer, J., Berry, R.F., Scott, R.J., Cooke, D.R., 2016. Arc-oblique fault systems: their role in the Cenozoic  
1075 structural evolution and metallogenesis of the Andes of central Chile. *Journal of Structural Geology*  
1076 89, 101-117.
- 1077 Piquer, J., Hollings, P., Rivera, O., Cooke, D.R., Baker, M., Testa, F., 2017. Along-strike segmentation of  
1078 the Abanico Basin, central Chile: New chronological, geochemical and structural constraints. *Lithos*  
1079 268, 174-197.
- 1080 Piquer, J., Skarmeta, J., Cooke, D.R., 2015. Structural Evolution of the Rio Blanco-Los Bronces District,  
1081 Andes of Central Chile: Controls on Stratigraphy, Magmatism, and Mineralization. *Economic Geology*  
1082 110, 1995-2023.
- 1083 Piquer, J., Yanez, G., Rivera, O., Cooke, D.R., 2019. Long-lived crustal damage zones associated with  
1084 fault intersections in the high Andes of Central Chile. *Andean Geology* 46, 223-239.
- 1085 Pommier, A., 2014. Interpretation of magnetotelluric results using laboratory measurements. *Surv*  
1086 *Geophys* 35, 41-84.
- 1087 Pritchard, M.E., Jay, J.A., Aron, F., Henderson, S.T., Lara, L.E., 2013. Subsidence at southern Andes  
1088 volcanoes induced by the 2010 Maule, Chile earthquake. *Nat Geosci* 6, 632-636.
- 1089 Ramos, V.A., 2010. The tectonic regime along the Andes: Present-day and Mesozoic regimes.  
1090 *Geological Journal* 45, 2-25.
- 1091 Ramos, V.A., Litvak, V.D., Folguera, A., Spagnuolo, M., 2014. An Andean tectonic cycle: From crustal  
1092 thickening to extension in a thin crust (34 degrees-37 degrees SL). *Geosci Front* 5, 351-367.
- 1093 Richards, J.P., Boyce, A.J., Pringle, M.S., 2001. Geologic evolution of the Escondida area, northern  
1094 Chile: A model for spatial and temporal localization of porphyry Cu mineralization. *Economic Geology*  
1095 and the *Bulletin of the Society of Economic Geologists* 96, 271-305.
- 1096 Roquer, T., Arancibia, G., Rowland, J., Iturrieta, P., Morata, D., Cembrano, J., 2017. Fault-controlled  
1097 development of shallow hydrothermal systems: Structural and mineralogical insights from the  
1098 Southern Andes. *Geothermics* 66, 156-173.
- 1099 Rowland, J.V., Sibson, R.H., 2004. Structural controls on hydrothermal flow in a segmented rift system,  
1100 Taupo Volcanic Zone, New Zealand. *Geofluids* 4, 259-283.
- 1101 Rowland, J.V., Simmons, S.F., 2012. Hydrologic, Magmatic, and Tectonic Controls on Hydrothermal  
1102 Flow, Taupo Volcanic Zone, New Zealand: Implications for the Formation of Epithermal Vein Deposits.  
1103 *Economic Geology* 107, 427-457.
- 1104 Sanchez, P., Perez-Flores, P., Arancibia, G., Cembrano, J., Reich, M., 2013. Crustal deformation effects  
1105 on the chemical evolution of geothermal systems: the intra-arc Liquine-Ofqui fault system, Southern  
1106 Andes. *International Geology Review* 55, 1384-1400.
- 1107 Sanchez-Alfaro, P., Sielfeld, G., Van Campen, B., Dobson, P., Fuentes, V., Reed, A., Palma-Behnke, R.,  
1108 Morata, D., 2015. Geothermal barriers, policies and economics in Chile - Lessons for the Andes. *Renew*  
1109 *Sust Energ Rev* 51, 1390-1401.
- 1110 SERNAGEOMIN, S., 2003. Mapa Geológico de Chile: versión digital. Servicio Nacional de Geología y  
1111 Minería, Publicación Geológica Digital, No. 4 CD-Room, versión 1.0, base geológica escala 1.
- 1112 Shaw, H.R., 1980. The fracture mechanisms of magma transport from the mantle to the surface.  
1113 *Physics of magmatic processes* 64, 201-264.
- 1114 Sibson, R.H., 1985. A Note on Fault Reactivation. *Journal of Structural Geology* 7, 751-754.
- 1115 Sibson, R.H., 1996. Structural permeability of fluid-driven fault-fracture meshes. *Journal of Structural*  
1116 *Geology* 18, 1031-1042.
- 1117 Sibson, R.H., 2004. Controls on maximum fluid overpressure defining conditions for mesozonal  
1118 mineralisation. *Journal of Structural Geology* 26, 1127-1136.

- 1119 Sielfeld, G., Cembrano, J., Lara, L., 2017. Transtension driving volcano-edifice anatomy: Insights from  
1120 Andean transverse-to-the-orogen tectonic domains. *Quaternary International* 438, 33-49.
- 1121 Sielfeld, G., Lange, D., Cembrano, J., 2019. Intra-Arc Crustal Seismicity: Seismotectonic Implications for  
1122 the Southern Andes Volcanic Zone, Chile. *Tectonics* 38, 552-578.
- 1123 Sillitoe, R., 1997. Characteristics and controls of the largest porphyry copper-gold and epithermal gold  
1124 deposits in the circum-Pacific region. *Australian Journal of Earth Sciences* 44, 373-388.
- 1125 Simpson, F., Bahr, K., 2005. *Practical magnetotellurics*. Cambridge University Press.
- 1126 Smith, J.D., White, R.S., Avouac, J.P., Bourne, S., 2020. Probabilistic earthquake locations of induced  
1127 seismicity in the Groningen region, the Netherlands. *Geophysical Journal International* 222, 507-516.
- 1128 Stanton-Yonge, A., Griffith, W.A., Cembrano, J., St Julien, R., Iturrieta, P., 2016. Tectonic role of margin-  
1129 parallel and margin-transverse faults during oblique subduction in the Southern Volcanic Zone of the  
1130 Andes: Insights from Boundary Element Modeling. *Tectonics* 35, 1990-2013.
- 1131 Stern, C.R., 2007. Chilean volcanoes. *The geology of Chile*, 147-178.
- 1132 Suzuki, Y., Ioka, S., Muraoka, H., 2014. Determining the Maximum Depth of Hydrothermal Circulation  
1133 Using Geothermal Mapping and Seismicity to Delineate the Depth to Brittle-Plastic Transition in  
1134 Northern Honshu, Japan. *Energies* 7, 3503-3511.
- 1135 Tardani, D., Reich, M., Roulleau, E., Takahata, N., Sano, Y., Perez-Flores, P., Sanchez-Alfaro, P.,  
1136 Cembrano, J., Arancibia, G., 2016. Exploring the structural controls on helium, nitrogen and carbon  
1137 isotope signatures in hydrothermal fluids along an intra-arc fault system. *Geochimica Et Cosmochimica*  
1138 *Acta* 184, 193-211.
- 1139 Tassi, F., Aguilera, F., Benavente, O., Paonita, A., Chiodini, G., Caliro, S., Agosto, M., Gutierrez, F.,  
1140 Capaccioni, B., Vaselli, O., 2016. Geochemistry of fluid discharges from Peteroa volcano (Argentina-  
1141 Chile) in 2010–2015: Insights into compositional changes related to the fluid source region (s).  
1142 *Chemical geology* 432, 41-53.
- 1143 Teyssier, C., Tikoff, B., Markley, M., 1995. Oblique Plate Motion and Continental Tectonics. *Geology*  
1144 23, 447-450.
- 1145 Tibaldi, A., 2005. Volcanism in compressional tectonic settings: Is it possible? *Geophysical Research*  
1146 *Letters* 32.
- 1147 Tikoff, B., Teyssier, C., 1994. Strain Modeling of Displacement-Field Partitioning in Transpressional  
1148 Orogens. *Journal of Structural Geology* 16, 1575-1588.
- 1149 Turienzo, M., Dimieri, L., Frisicale, C., Araujo, V., Sanchez, N., 2012. Cenozoic structural evolution of  
1150 the Argentinean Andes at 34 degrees 40 ' S: A close relationship between thick and thin-skinned  
1151 deformation. *Andean Geology* 39, 317-357.
- 1152 Veloso, E.E., Tardani, D., Elizalde, D., Godoy, B.E., Sanchez-Alfaro, P.A., Aron, F., Reich, M., Morata, D.,  
1153 2019. A review of the geodynamic constraints on the development and evolution of geothermal  
1154 systems in the Central Andean Volcanic Zone (18-28 degrees Lat.S). *International Geology Review*.
- 1155 Viramonte, J., Galliski, M., Saavedra, V.A., Aparicio, A., García-Cacho, G., Escorza, C.M., 1984. El  
1156 finivolcanismo básico de la depresión de Arizaro, provincia de Salta. IX Cong. Geol. A rg., Actas 3, 234-  
1157 251.
- 1158 Waldhauser, F., Ellsworth, W.L., 2000. A double-difference earthquake location algorithm: Method  
1159 and application to the northern Hayward fault, California. *Bulletin of the Seismological Society of*  
1160 *America* 90, 1353-1368.
- 1161 Wannamaker, P.E., Caldwell, T.G., Jiracek, G.R., Maris, V., Hill, G.J., Ogawa, Y., Bibby, H.M., Bennie,  
1162 S.L., Heise, W., 2009. Fluid and deformation regime of an advancing subduction system at  
1163 Marlborough, New Zealand. *Nature* 460, 733-736.
- 1164 Wrage, J., Tardani, D., Reich, M., Daniele, L., Arancibia, G., Cembrano, J., Sanchez-Alfaro, P., Morata,  
1165 D., Perez-Moreno, R., 2017. Geochemistry of thermal waters in the Southern Volcanic Zone, Chile -  
1166 Implications for structural controls on geothermal fluid composition. *Chemical Geology* 466, 545-561.
- 1167 Yáñez, G.A., Gana, P., Fernández, R., 1998. Origen y significado geológico de la Anomalía Melipilla,  
1168 Chile central. *Revista geológica de Chile* 25, 175-198.
- 1169